Optimizing THz generation from a spintronic emitter for field-driven applications at MHz repetition rates

Master Thesis

submitted by

Alkisti Vaitsi

Fachbereich Physik
Freie Universität Berlin

Berlin, January 24, 2022

This work was performed between July 2020 and July 2021 in the Ultrafast Scanning Probe Microscopy Research Group headed by Dr. Melanie Müller, associated with the Department of Physical Chemistry (headed by Prof. Dr. Martin Wolf) at the Fritz Haber Institute of the Max Planck Society.

Primary Supervisor: Prof. Dr. Tobias Kampfrath

Secondary Supervisor: Priv.-Doz. Dr. Albrecht Lindinger

Date of submission: January 24, 2022

Introduction

The terahertz (THz) radiation covers the frequency range from 0.1 to 30 THz in the electromagnetic spectrum, which is situated between the realms of electronics and optics [FZ02]. During the last decades, the THz frequency region has increasingly drawn the interest of numerous research communities, such as physics, chemistry, material science, and medicine. Combined with technological improvements in the fields of photonics and optics, plentiful applications of the THz radiation in a variety of directions have emerged [Ton07], [Mit17]. That increasing interest is due to the fact that THz photon energies can couple resonantly to many elementary processes in all states of matter. In solids, for example, phonos, spin resonances, excitons, plasma frequencies, and superconducting gaps exist in this frequency range.

In this work, the produced THz pulsed radiation is intended to be employed for realizing a newly developed ultrafast scanning tunneling microscopy technique called THz-STM. That technique gives access to various spatio-temporal phenomena and enables the study of ultrafast dynamics of optical excited systems, such as nanostructures and molecules at surfaces, with femtosecond temporal and atomic-level spatial resolution [THKH21], [MSKW20].

THz-gated Scanning Tunneling Microscopy (THz-STM)

In THz-gated scanning tunneling microscopy, the electric field of a single-cycle THz pulse acts as a quasi-static bias voltage modulation of the STM junction, resulting in a time-dependent current response. Thus, coupling THz pulses to the STM junction allows for control of tunneling currents on femtosecond time scales, maintaining the spatial resolution of the STM. For the STM photoexcitation, to get measurable currents, an essential ingredient is the high repetition rate of the laser source. For that purpose, near-infrared ultrashort laser pulses of a broadband OPCPA (Optical Parametric Chirped-pulse Amplification) laser system are employed. It is an amplified laser system, which delivers ∼8 fs laser pulses centered at 800 nanometers. It operates with a variable high repetition rate of 0.5 MHz or 1 MHz, resulting in 6 μJ or 3 μJ pulse energies, respectively. Moreover, achieving

high time resolution in THz-STM requires shorter THz pulse width, which in turn requires a broadband THz spectrum. In this regard, the spintronic THz emitter (STE) is employed as the source of radiation. Compared to THz sources regularly used, such as nonlinear optical crystals (GaP, ZnTe) and high-performance photoconductive switches, the STE provides a significant advantage: it delivers ultrabroadband single-cycle THz pulses with a frequency spectrum covering the range from 1 to 30 THz without a gap [SJM+16], [SJS+17]. Due to its fast transients and extremely large bandwidth, the STE is a very well-suited THz source for THz-STM as it enables very fast voltage modulation in the STM, increasing the achievable time resolution. Further advantages are the easy THz polarity flipping and easy polarization control through the applied STE magnetization.

This thesis

This work aims to optimize the excitation conditions of the spintronic emitter employed for THz-STM measurements and achieve high THz field amplitudes onto the STM tip at MHz repetition rates and microjoule pulse energies. The initial curved-wavefront excitation geometry for the spintronic emitter, combined with the employed laser parameters, gives rise to several unwanted effects, reducing the THz emission and propagation efficiency. In a first step, the attempt to disentangle those effects and then define design considerations for a new optimized excitation geometry is presented. For that purpose, measurements and numerical simulations of the THz propagation through optical systems are performed. Consequently, a new optimized excitation geometry is designed and built based on the acquired knowledge. It consists of a plane-wavefront excitation geometry and gives the flexibility to test variable pump spot sizes for the STE. In the new experimental setup, several measurements are performed that help to conclude the ideal condition that leads to higher THz fields onto the STM tip. The results are discussed and presented in the final part of this thesis.

Contents

Chapter 1

Theoretical background

Optical fields, in particular near-infrared femtosecond laser pulses, are employed to excite the spintronic THz emitter. The delivered THz pulses have an ultrabroadband spectrum giving rise to several challenging issues regarding their spatial characteristics and efficient propagation through the optical systems. In the course of this work, numerical simulations modeling the propagation of the THz spectrum through different optical systems and under different excitation conditions are performed. The simulations provide insights for understanding experimental results, and in turn, directions for constructing a new, optimized excitation geometry for the spintronic emitter. This chapter presents the theoretical background and formalism used for this purpose. In Section 1.1, the angular spectrum representation method is introduced. It is a powerful technique for describing laser beam propagation and light focusing. In the paraxial limit, this approach leads to the derivation of Gaussian beams, which are described in Section 1.2. Lastly, in Section 1.3 the ABCD matrix analysis is presented, which is the mathematical method employed for calculating the evolution of a Gaussian beam through an optical system. In all numerical simulations conducted during this work, both the optical and THz fields are modeled as Gaussian beams. The discussion below relies on references [NH06],[ST19],[Sve10],[Kog65],[ald15].

1.1 Propagation of optical fields: angular spectrum representation

The angular spectrum representation is a mathematical approach for modeling light propagation in homogeneous optical media. This technique has

its origins in Fourier optics [Goo05], [ST19]. Under this formalism, any arbitrary optical field can be described as a superposition of plane waves with variable amplitudes, pointing in different directions in space. The fields are evaluated in planes that are perpendicular to the propagation axis z (see Fig. 1.3). Thus, assuming that one knows the field $\vec{E}(\vec{r})$ at an arbitrary point $\vec{r} = (x, y, z)$, the question would be: how could that field be calculated in an arbitrary destination plane z=constant?

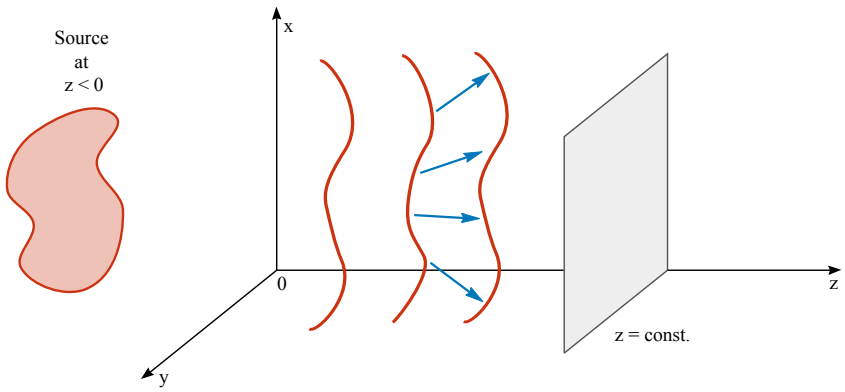

Figure 1.1: Assuming a light source at $z < 0$, under the angular spectrum representation the propagated field is evaluated in planes perpendicular to the propagation axis z.

One starts by decomposing the field within an initial z plane into a sum of two-dimensional plane waves as

$$\vec{E}(x, y, z) = \frac{1}{2\pi} \int_{-\infty}^{\infty} \int_{-\infty}^{\infty} \vec{E}(k_x, k_y; z) e^{i[k_x x + k_y y]} dk_x dk_y \tag{1.1}$$

where x, y are the Cartesian transverse coordinates and k_x, k_y are the reciprocal coordinates or spatial frequencies, respectively. Each plane wave has a weight $\vec{E}(k_x, k_y; z)$, which is called the angular spectrum of the filed and it is related to the $\vec{E}(x, y, z)$ via a two-dimensional spatial Fourier transform:

$$\vec{E}(k_x, k_y; z) = \frac{1}{2\pi} \int_{-\infty}^{\infty} \int_{-\infty}^{\infty} \vec{E}(x, y, z) e^{-i[k_x x + k_y y]} dx dy. \tag{1.2}$$

Both the field and its angular spectrum are vectors, implying that the Fourier integrals hold independently for each vector component. Therefore, each plane wave is propagated separately through the Fourier domain to the destination plane. How could this propagation be evaluated?

Assuming an isotropic, homogenous, linear and source-free medium in the transvesre plane, a time-harmonic, optical field has to fulfil the vector Helmholtz equation

$$(\nabla^2 + k^2)\vec{E}(\vec{r}) = 0 \tag{1.3}$$

where the wavenumber k is determined by the dispersion relation $c^2k^2 = \omega^2 n^2$, with c being the speed of light, ω the angular frequency of the field, and $n = \sqrt{\mu\epsilon}$ the refractive index of the medium. Substituting the Fourier representation of the electric field $\vec{E}(x, y, z)$ (Eq.1.1) into the Helmholtz equation (Eq.1.3), and assuming that we know the field in the plane z=0, then the angular spectrum of the optical filed at a destination plane z, will be

$$\vec{E}(k_x, k_y; z) = \vec{E}(k_x, k_y; z = 0)e^{ik_z z} \tag{1.4}$$

where k_z is given by the formula

$$k_z = \pm\sqrt{k^2 - (k_x^2 + k_y^2)}. \tag{1.5}$$

The longitudinal component of the wave vector k_z is fixed by the length of the wave vector k. The $'\pm'$ sign determines whether the field propagates in the positive or negative z-direction, which depends on whether the field source is located before or after the plane z=0, where it is assumed that the electric field is known.

From the Eq.1.4, one sees that the spatial spectrum of the electric field in an arbitrary destination plane z, is uniquely defined by multiplying the spectrum in the initial plane z=0 by the factor

$$H(k_x, k_y; z) = e^{\pm ik_z z}. \tag{1.6}$$

This factor, in the reciprocal space, is called *propagator* or *optical transfer function* (OTF) of free space.

After propagating each plane wave through the Fourier domain, all the plane waves will be added back together, and the wavefield in the arbitary destination plane z will be reconstructed via an inverse spatial Fourier transform. Inserting the result of Eq.1.4 into Eq.1.1 we finally have

$$\vec{E}(x, y, z) = \frac{1}{2\pi}\int_{-\infty}^{\infty}\int_{-\infty}^{\infty}\vec{E}(k_x, k_y; z = 0)e^{ik_z z}e^{ik_x x + ik_y y}dk_x dk_y \tag{1.7}$$

which is known as the *angular spectrum representation* (ASR).

1.1.1 Evanescent field

A particular result that follows from the angular spectrum method is the existence of evanescent fields, which are relevant to this work. For the generation of THz radiation, optical fields are used. Between those two regimes of the electromagnetic spectrum, there is a considerable variation in wavelengths. The THz wavelengths range from 300 μm to 3 μm and are orders of magnitude longer than the wavelengths of the optical regime, which are centered around 800 nm. This mismatch can result in THz emission from subwavelength volumes, leading to evanescent waves on the emitter's surface.

To understand the evanescent fields better, one needs to take a closer look at the propagator of Eq.1.6, which contains all the information about the optical medium, and therefore, how the light propagates through it. Assuming a purely dielectric medium with no losses, the refractive index n is a real and positive quantity. Thus, the same holds true for the wave vector k. Hence, the longitudinal component of the wave vector k_z (Eq.1.5) is either real or imaginary and converts the factor $exp(ik_z z)$ into an oscillatory or exponentially decaying function, respectively. Therefore, two possible characteristic solutions can occur for a specific (k_x, k_y) pair

$$\begin{aligned} \text{Plane waves}: \quad & e^{i[k_x x + k_y y]} e^{ik_z z}, \quad k_x^2 + k_y^2 \leq k^2 \\ \text{Evanescent waves}: \quad & e^{i[k_x x + k_y y]} e^{-k_z z}, \quad k_x^2 + k_y^2 > k^2. \end{aligned} \tag{1.8}$$

A graphical representation will help to analyze the results above. The equation $k_x^2 + k_y^2 = k^2$ describes a circle with radius k. Thus, one can identify the circle with radius k in the reciprocal space, as is depicted in Fig.1.2. For all the k vectors inside the circle ($k_x^2 + k_y^2 \leq k^2$), the expression under the square root of Eq.1.5 is positive, thus the k_z is real. The propagator then becomes an oscillating function in z. On the other hand, for all the k vectors outside the circle ($k_x^2 + k_y^2 > k^2$), the expression under the square root of Eq.1.5 is negative; thus, the k_z is imaginary. As a consequence, the propagator of Eq.1.6 becomes an exponential decay along the propagation axis z. This means that all the spatial frequencies inside the circle with radius k are plane waves that can propagate in the far-field. In contrast, all the spatial frequencies outside the circle decay exponentially along the z-axis, and they stand for the evanescent waves. The spatial range where the evanescence waves still exist is called near-field, and that is for a distance less than a wavelength. Therefore, if the destination plane is located in the far-field

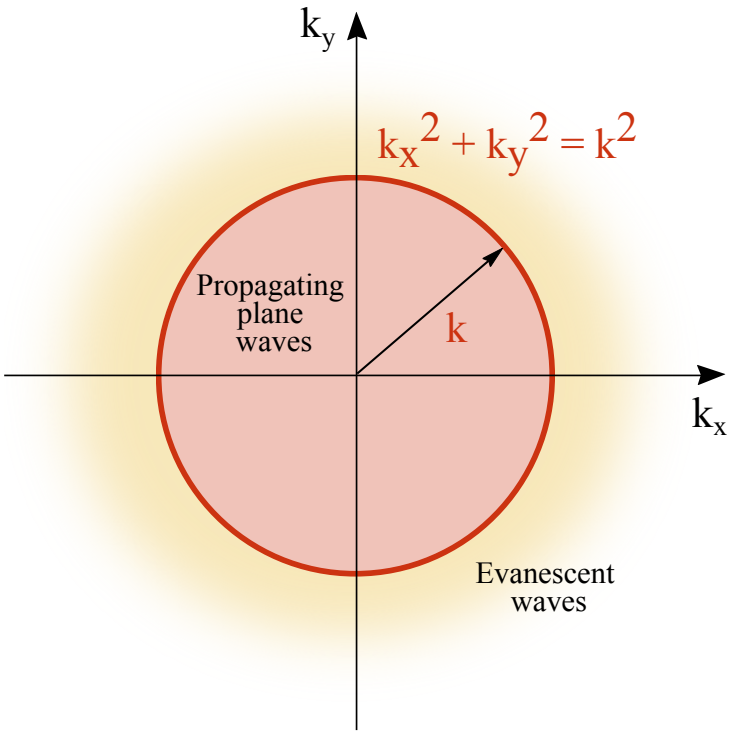

Figure 1.2: Reciprocal space. The red circle presents the value of k. The wavevectors of the propagating plane waves are restricted to the circle area, while the wavevectors of the evanescent waves are extended outside of it.

($\gg \lambda$), the contribution of the decaying components (evanescent waves) is zero.

1.1.2 Paraxial approximation

In the case of a collimated or a weakly focused laser beam, as the light propagates along a certain direction z, it spreads out slightly in the transverse plane. For those cases, in the angular spectrum representation, the wavevectors $\vec{k} = (k_x, k_y, k_z)$ are almost parallel to the propagation axis z and the transverse components (k_x, k_y) are small in comparison to k. Thus, the so-called paraxial approximation can be applied, under which the square root of Eq. 1.5 can be expanded in a series as

$$k_z = k\sqrt{1 - (k_x^2 + k_y^2)/k^2} \approx k - \frac{(k_x^2 + k_y^2)}{2k}. \tag{1.9}$$

This approximation significantly simplifies the Fourier integrals, and it is applied to derive the following formalism of the Gaussian laser beams, which are considered in cases where the beam divergence is relatively small.

1.2 Gaussian beams

All the numerical simulations performed during this work model the optical field used for the excitation of the spintronic emitter and the resulting THz radiation as Gaussian beams.

A Gaussian beam is the fundamental (or TEM_{00}) mode of many laser sources and often the most desirable output. Mathematically, it occurs as a solution to the paraxial Helmholtz equation (Eq. 1.3). It is a beam of monochromatic electromagnetic radiation, characterized by a Gaussian irradiance profile in any plane transverse to the direction of propagation. Thus, assuming a 2-D light beam, meaning that the light propagates in the z-direction and the electric field oscillates in only one transversal direction r, the field distribution, near the optical axis (z-axis), is given by the paraxial representation of a Gaussian beam

$$\vec{E}(r,z) = \vec{E}_o \frac{w}{w_o} exp\left[-i(kz + \phi(z))\right] exp\left[-i\frac{kr^2}{2R(z)} - \frac{r^2}{w^2(z)}\right] \tag{1.10}$$

where E_0 is a constant field vector in the transverse (x,y) plane, r is the radial distance away from the propagation axis ($r^2 = x^2 + y^2$), w_o is the beam waist, where the transversal beam size is minimum and z is the propagation distance from the beam waist plane. $k = \frac{2\pi}{\lambda}$ is the wavenumber, and λ is the wavelength of light inside the medium where the beam propagates. $w(z)$ is the beam radius and $R(z)$ is the radius of curvature of the phase front. $\phi(z)$ is the Gouy phase shift, which indicates an additional phase shift related to the geometry of the beam. The last three parameters will be discussed in detail later.

In Eq.1.10, the exponential term consists of a real and an imaginary part. The imaginary part contains information about the beam phase, and the real part is associated with the transversal irradiance (or intensity) profile. Thus, as the intensity is the square modulus of the electric field amplitude distribution, the real part of the Eq.1.10 is extracted, and the following relationships occur:

$$E(r,z) \propto exp\left[-\frac{r^2}{w^2(z)}\right] \tag{1.11}$$

$$I(r,z) = |E(r,z)|^2 \propto exp\left[-\frac{2r^2}{w^2(z)}\right]. \tag{1.12}$$

In Fig.1.3, it becomes apparent that the intensity distribution (as well as the field distribution) is symmetric around the beam center and decreases as the radial distance increases.

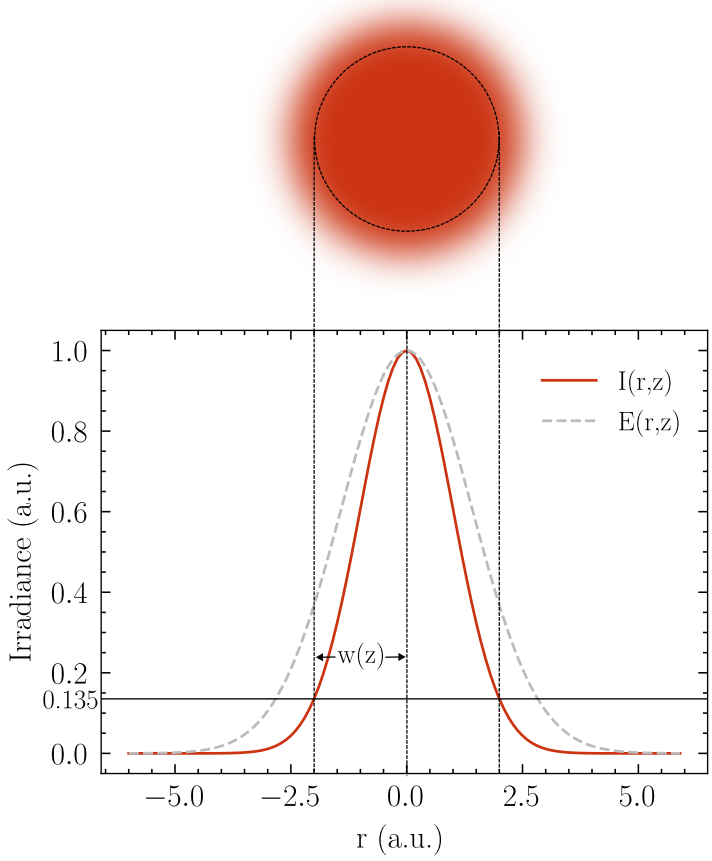

Figure 1.3: Gaussian beam amplitude and Irradiance. The transverse irradiance profile (solid line) and the electric field amplitude distribution (dashed line) of a Gaussian beam are depicted. Both curves are normalized to the maximum value. The horizontal line indicates the $1/e^2$ of the maximum intensity, the location where the beam radius is defined.

As the light beam propagates through space, the transverse irradiance

distribution remains Gaussian but is not constant, therefore there is a dependence of $w(z)$ on z. Due to diffraction, the beam will converge towards and diverge away from the beam waist w_o, which is the area where the beam radius reaches its minimum value, and similarly where the on-axis intensity ($r = 0$) is the greatest. The graphical representation of a paraxial Gaussian beam is depicted in Fig.1.4.

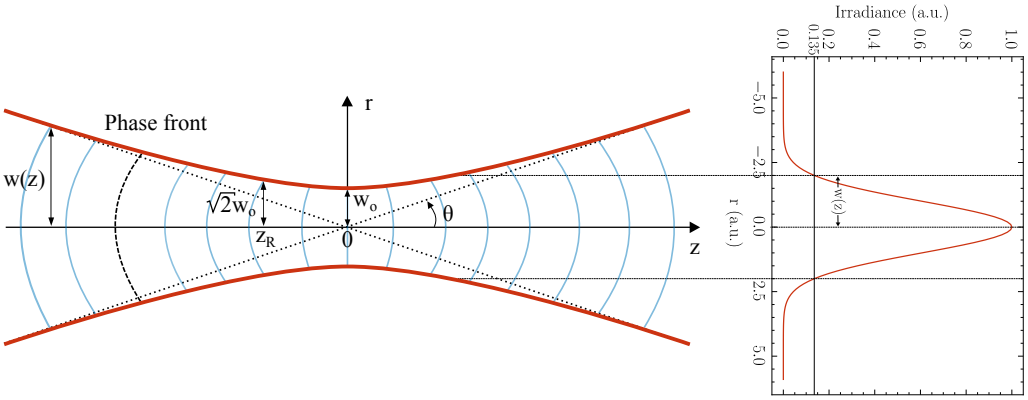

Figure 1.4: Graphical representation of a paraxial Gaussian beam. The hyperbolic red lines represent the evolution of the beam radius through the propagation axis. As the beam propagates away from the beam waist, it acquires an approximately spherical phase wavefront (light blue curves). The transversal Gaussian irradiance distribution is preserved along the propagation axis.

The beam radius w(z) is defined as the location where the intensity drops to $1/e^2$ (13.5%) of its maximum value (Fig.1.3), and its evolution along the propagation axis is given by:

$$w(z) = w_o \sqrt{1 + \left(\frac{z\lambda}{\pi w_o^2}\right)^2}. \tag{1.13}$$

When the beam propagates towards infinity ($z = \pm\infty$), it expands symmetrically in both directions from the beam waist by the divergence angle:

$$\theta \cong tan\theta = \frac{\lambda}{\pi w_0} \tag{1.14}$$

where the paraxial approach is used ($\theta \ll 1\ rad$). From the last equation, one can see that the beam's divergence and the beam waist are reciprocal parameters. This implies that a well-collimated beam (small divergence angle)

will be achieved when the beam waist is large. On the other hand, a tightly focused beam will result in a high divergence. It is worth noting that θ also depends on λ, which is the wavelength of light inside the medium where the beam propagates. Thus, assuming a constant beam waist, light with lower frequencies will diverge more than light with higher frequencies.

Proceeding with the analysis of the field distribution, and now focusing on the imaginary part of the exponential in Eq.1.10, the transverse phase factor:

$$exp\left[-i\frac{kr^2}{2R(z)}\right]$$

shows a quadratic dependence on r. This originates from the paraxial approach of a spherical wavefront with radius R(z). Accordingly, the function R(z) is representing the radius of curvature of the phase front of the Gaussian beam, and it evolves along the propagation axis as:

$$R(z) = z\left[1 + \left(\frac{\pi w_o^2}{z\lambda}\right)^2\right]. \tag{1.15}$$

In Fig.1.5 the Eq.1.15 is plotted. One sees that when z tends to infinity, then $R \approx z$. This would be the typical behavior of a spherical wavefront coming from a point source, originated at $z = 0$. The linear equation $R(z) = z$ is also plotted as a dashed line. However, for z=0, the radius of curvature of the Gaussian beam is infinity. This implies that at the beam waist, the wavefront is plane. Thus, starting from the beam waist, as plane wavefront, the radius of curvature decreases from infinity to a minimum value and then increases linearly with z, just as for a spherical wave, being a plane wavefront again at $z = \pm\infty$.

The point where the radius of curvature reaches its minimum value (the largest curvature) is when $z = z_R$, where z_R is known as the Rayleigh range, and it is defined as:

$$z_R = \frac{\pi w_0^2}{\lambda}. \tag{1.16}$$

At $z = z_R$, the beam radius is larger than in the beam waist by a factor of $\sqrt{2}$; hence, one can say that the beam size in the Rayleigh range is nearly constant and start increasing linearly for $z > z_R$ (that is, approaching the dashed line in Fig.1.4). Thus, it should also be noted that the value of the Rayleigh length indicates how the beam diverges, i.e., the largest the value

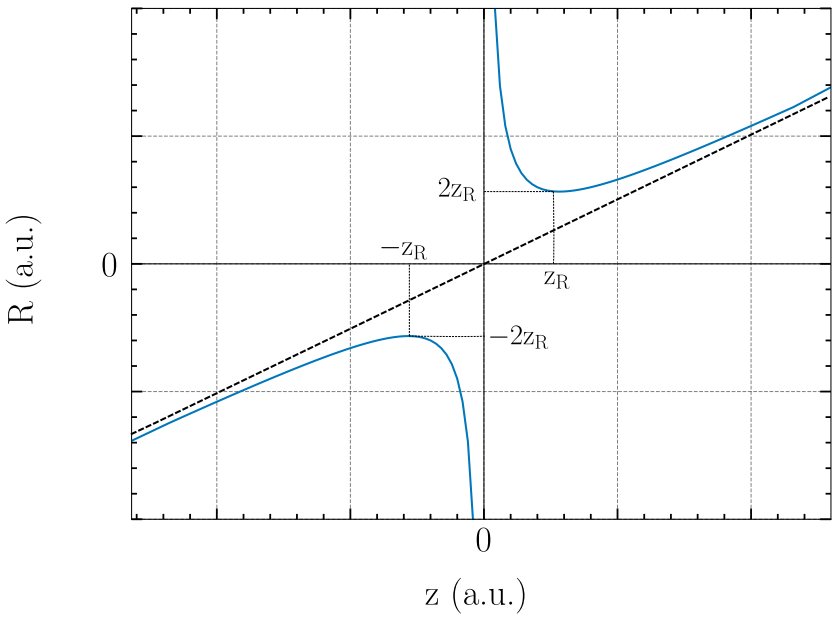

Figure 1.5: Radius of curvature. At the distances of $\pm z_R$ from the beam waist plane, the radius of curvature reaches the minimum of its absolute value. At the beam waist, the wavefront is plane, i.e., the radius of curvature is infinity. The dashed line depicts the radius of curvature of a spherical wavefront coming from a point source, originated at $z = 0$.

of z_R the later the beam will start to expand linearly.

Lastly, in Eq.1.10 there is also a longitudinal phase factor:

$$exp\left[-i(kz + \phi(z))\right].$$

Along the propagation axis, other than the phase shift (kz) of a plane wave, the Gaussian beam obtains an additional phase term $\phi(z)$, which is called Gouy phase shift, and it is given by:

$$\phi(z) = arctan(\frac{z}{z_R}). \tag{1.17}$$

The plot in Fig. 1.6 depicts the evolution of $\phi(z)$ along the z-axis. The Gouy phase shift changes from $(-\pi/2)$ to $(\pi/2)$. Thus, overall, it represents a π phase shift when the Gaussian beam wavefront crosses the beam waist plane.

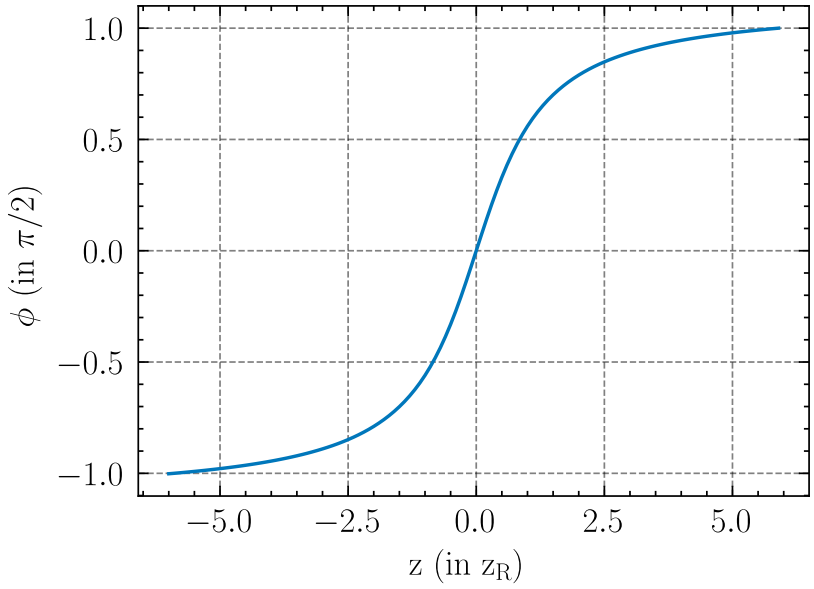

Figure 1.6: Gouy phase shift. The Gouy phase shift asymptotes to $\pm\pi/2$ as z tends to $\pm\infty$. Therefore, the overall phase shift from $z = -\infty$ to $z = +\infty$ is π.

A Gaussian beam can be described as a superposition of many plane waves with k vectors propagating in different directions. The plane wave components which do not propagate parallel with the beam axis undergo smaller phase shifts in the z-direction. Thus, it is expected that the phase shift of a Gaussian beam is not identical to that of a plane wave.

For a Gaussian beam, both the spot size $w(z)$ and the radius of curvature $R(z)$, can be described by the so-called complex beam parameter or complex radius of curvature, which is given by

$$\frac{1}{q(z)} = \frac{1}{R(z)} - i\frac{\lambda}{\pi w^2(z)}. \tag{1.18}$$

By substituting the depedencies of $w(z)$ (Eq.1.13) and $R(z)$ (Eq.1.15), one can obtain an alternative expression:

$$q(z) = z + iz_R. \tag{1.19}$$

Utilizing the complex beam parameter the electric field of the Eq. 1.10

can be written as

$$\vec{E}(r,z) = \frac{\vec{E}_o}{q(z)} exp\left[-ik\frac{r^2}{2q(z)}\right] exp[-ikz]. \tag{1.20}$$

Furthermore, the definition of the complex beam parameter simplifies the mathematical formalism of the Gaussian beam propagation through an optical system, and the ABCD matrix analysis can be introduced.

1.3 ABCD matrix analysis of Gaussian beams

The ABCD matrix analysis (or ray transfer matrix analysis) originates from the geometrical optics, where it is used for calculating the propagation of light rays through optical elements [ST19], [Sie86]. However, it can also be utilized to calculate the evolution of propagating Gaussian beams that we are interested in.

Within the paraxial approach, an ABCD matrix is a 2x2 matrix related to an optical element and describes the effect of the element on a light beam. A light beam usually propagates through multiple sequential optical elements, including the propagation through air, meaning through an optical system. The ABCD matrix of an optical system is the matrix product of all the single matrices corresponding to the successive system's components.

Considering a Gaussian beam which enters and then propagates through an optical system, its initial complex radius of curvature q_{in} (Eq.1.18), changes according to the ABCD law:

$$q_{out} = \frac{Aq_{in} + B}{Cq_{in} + D}. \tag{1.21}$$

From the resulting complex radius of curvature q_{out}, the new beam parameters, i.e., the beam radius w_{out} and the radius of curvature R_{out} of the wavefronts can be then extracted. Fig. 1.7 shows a scheme of this description.

Two important examples that are employed in this work are:

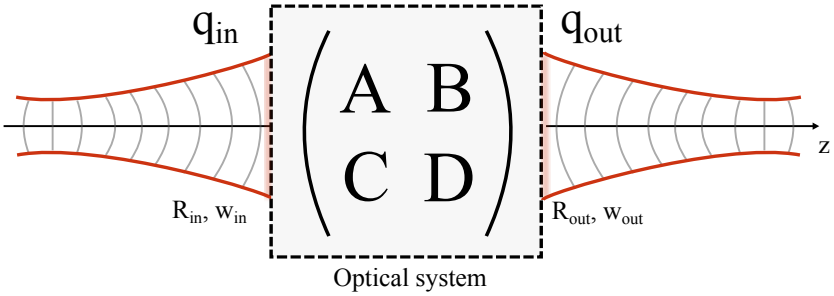

Figure 1.7: ABCD law for Gaussian beams. An optical system is represented by its ABCD matrix, which describes the effect of the system in the ingoing light beam. The initial complex radius of curvature q_{in} of the Gaussian input beam will change according to the ABCD law (Eq. 1.21), resulting in the new complex radius of curvature q_{out}. The new complex beam parameter contains the information of the new beam radius $w(z)_{out}$ and radius of curvature $R(z)_{out}$ of the outgoing Gaussian beam.

- **Propagation in free space by z=d**
  Given a beam traveling a distance d through the free space, the ABCD matrix is
  $$\hat{M}_{air} = \begin{pmatrix} 1 & d \\ 0 & 1 \end{pmatrix} \tag{1.22}$$
  and thus, by substituting it in Eq 1.21
  $$q_{out} = q_{in} + d. \tag{1.23}$$

- **Propagation through a thin lens with focal lenght f**
  Given a beam traveling through a thin lens with focal length f, the ABCD matrix is
  $$\hat{M}_{lens} = \begin{pmatrix} 1 & 0 \\ -1/f & 1 \end{pmatrix} \tag{1.24}$$
  and thus, by substituting it in Eq 1.21
  $$\frac{1}{q_{out}} = \frac{1}{q_{in}} - \frac{1}{f}. \tag{1.25}$$

Chapter 2

Experimental details

In the course of this work, two different excitation geometries for the spintronic THz emitter are investigated and discussed. The experimental setups are described separately in detail in the following two chapters. However, this chapter provides experimental details common in both geometries. First, in Section 2.1 the employed laser source is described. Then, Section 2.2 presents the core mechanism of the spintronic THz emitter, its properties and advantages for THz-STM applications. Last, the used THz detection method, electro-optic sampling, is described in Section 2.3.

2.1 Laser system

The employed laser system (commercially available) is based on an octave-spanning, mode-locked Ti:Sapphire oscillator (VenteonPulse One), which seeds a Yb-fiber laser amplifier and a two-stage optical parametric chirped-pulse amplifier (venteon OPCPA). It delivers ultrashort laser pulses with duration of ∼8 fs and a central wavelength of 800 nm. It can operate at a variable repetition rate of 0.5 MHz or 1 MHz, resulting in 6 μJ or 3 μJ pulse energies, respectively. In both cases, the averag power is reaching 3 W. In Fig. 2.1 a schematic of the laser system is demonstrated.

A continuous-wave (CW) green laser (Coherent Verdi) pumps the mode-locked Ti:Sapphire oscillator. This system produces an octave-spanning output at an 80 MHz repetition rate delivering few-cycle laser pulses of ∼5 fs. From its ultrabroadband output spectrum, a narrowband spectral component at 1030 nm is filtered out and directed to the fiber amplifier stages (pre-amplifier and main-amplifier). The pulses are picked, stretched, am-

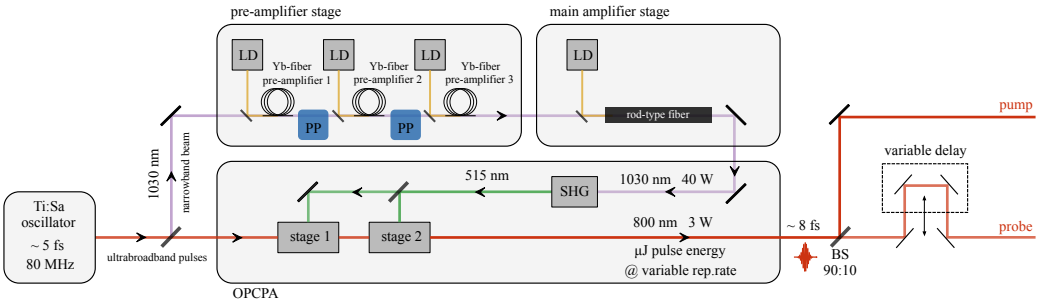

Figure 2.1: Schematic of the laser system. From the output spectrum of an 80 MHz octave-spanning, mode-locked Ti:Sapphire oscillator, a narrowband beam of 1030 nm is filtered out and directed to the four stages fiber amplifiers (three Yb-fiber pre-amplifiers and one rod-type fiber main amplifier). The pulse pickers (PP), in the pre-amplifier stage, enable the variation of the repetition rate of the laser system. In the main amplifier stage, the beam obtains the most of its energy, and after that, it is frequency-doubled by second harmonic generation (SHG). The produced beam seeds the two optical parametric amplifier stages, leading to an energy transfer from the amplified narrowband beam to the ultrabroadband pulses through a phased matched process. The 90% of the output power is available for the experiments, and from this, the beam is split at a ratio of 90:10 to the pump (THz generation, see Section 2.2) and the probe (THz detection, see Section 2.3) path, respectively. The figure is redrawn from [Mal17].

plified, recompressed, then frequency-doubled, and recombined with the ultrabroadband pulses in the OPCPA stage. Therefore, one can describe the amplification process in four stages: three Yb-fiber pre-amplifiers and one rod-type main amplifier. After the first and second pre-amplifier, the pulse pickers enable the variation of the repetition rate between 0.5 MHz and 1 MHz. After the third pre-amplifier the laser beam is directed to the main amplifier stage passing the rod-type fiber, from which it gains the most of its energy (40 W). In the nonlinear crystal, through second harmonic generation (SHG), the light is frequency-doubled and a laser beam with a wavelength of 515 nm is generated. This beam pumps the two-stage optical parametric amplifier, resulting in an energy transfer from the amplified narrowband beam to the ultrabroadband pulses through a phased matched process. Finally, the output is ultrabroadband few-cycle laser pulses of ∼8 fs duration, 800 nm central wavelength, with μJ pulse energy at variable repetition rates, delivering 3 W average power. The 90% of the output power is available for our setup, and from this, the beam is split at a ratio of 90:10 to seed the THz generation (pump) and detection path (probe), respectively (see Sections 2.2

and 2.3). In Fig. 2.2, the output spectrum of the laser system is depicted.

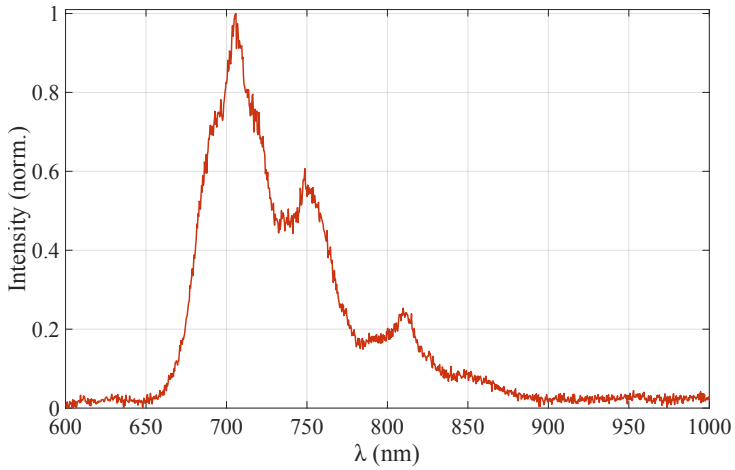

Figure 2.2: Output spectrum of the laser system

2.2 Spintronic THz emitter

The spintronic THz emitter is a novel source of THz radiation, and it was first demonstrated in 2013 [KBM+13]. Its core mechanism is based on spin-to-charge current conversion, namely the inverse spin-Hall effect. Figure 2.3 depicts its basic principle.

In this bilayer structure, composed of a ferromagnetic (FM) and a non-ferromagnetic (NM) metal thin film (few nanometers), the FM layer is magnetized in-plane by an external magnetic field $\overrightarrow{M}$. When illuminated by an incident ultrafast femtosecond laser pulse, electrons in the metals are promoted to states above the Fermi energy, resulting in non-equilibrium electron distribution, thus altering their band velocity and scattering rate. The FM and NM layers have different transport properties, which gives rise to a net current along the z-axis. Furthermore, in the FM metal, the photoexcited spin-up (majority) electrons have much higher mobility than that of the spin-down (minority) electrons, and as a consequence, the z current is spin-polarized [KBM+13], [ZCE06]. When this impulsive spin-polarized current j_s is injected into the NM layer, due to the spin-orbit interaction, electrons will 'feel' an effective magnetic field. Since this effective magnetic field is opposite for spin-up and spin-down electrons, they will be deflected in opposite directions with a mean angle γ. This is the inverse spin-Hall effect

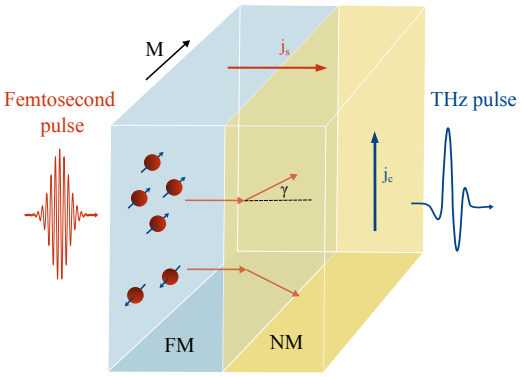

Figure 2.3: Spintronic terahertz emitter. A stack of a ferromagnetic (FM) and a nonmagnetic (NM) metal thin film is excited by an optical femtosecond laser pulse. The FM layer is magnetized homogeneously by an external magnetic field. The excitation launches spin transport from the FM into the NM layer, where the longitudinal spin current is converted into an ultrafast transverse charge current, leading to the emission of a THz electromagnetic pulse. Figure redrawn from [SJM+16]

(ISHE). Because of this, the longitudinal (z-directed) spin current density j_s is converted into an ultrafast transverse (x-directed) charge current density $j_c = \gamma j_s$. The transient j_c acts as an electric dipole, oscillating on the femtosecond time scale, leading to the emission of pulsed terahertz (THz) electromagnetic radiation into free space.

After extensive research for maximizing the THz output and tailoring the THz emission dynamics, a trilayer version of the STE was demonstrated in 2016 [SJM+16]. In contrast to the FM/NM bilayer structure, which uses only the forward spin current, the trilayer version (NM/FM/NM) also takes advantage of the backward spin current, leading to 40% higher THz amplitudes. A 5.8 nm thick W/CoFeB/Pt trilayer spintronic emitter grown on 500 μm sapphire substrate is employed for this work.

All previously presented terahertz emitters have exploited exclusively the charge but not the spin of electrons. Compared to THz sources regularly used, such as nonlinear optical crystals (GaP, ZnTe) and high-performance photoconductive switches, the STE provides a significant advantage: it delivers ultrabroadband single-cycle THz pulses with a frequency spectrum covering the range from 1 to 30 THz without a gap (see Fig. 2.4) [SJM+16], [SJS+17]. The resulting THz pulse shape and the spectral bandwidth are determined by the pump pulse duration and the induced carrier dynamics in the STE

[NSS+19]. Due to its fast transients and extremely large bandwidth, the STE is a very well-suited THz source for THz-STM as it enables very fast voltage modulation in the STM, increasing the achievable time resolution. In

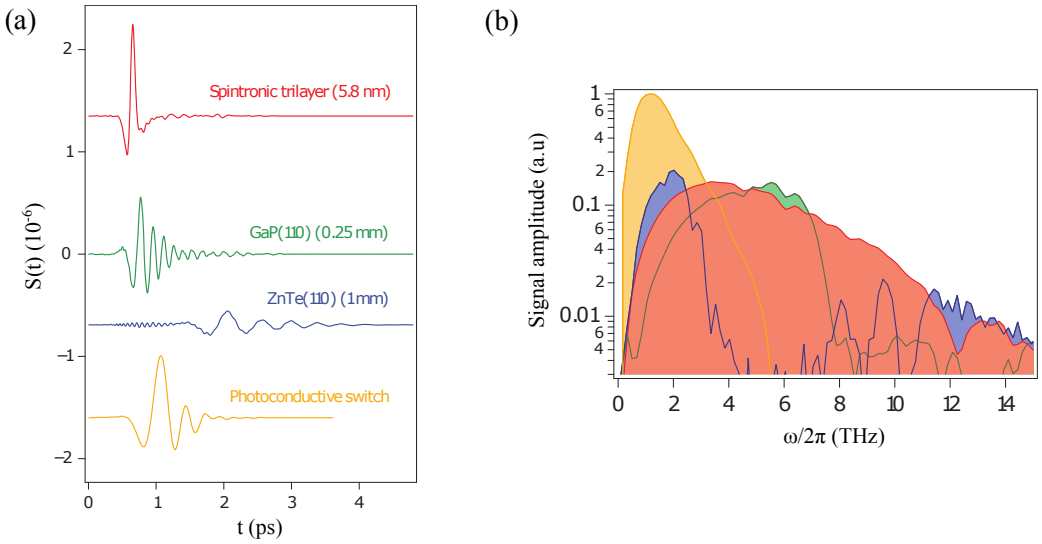

Figure 2.4: (a) THz waveforms and **(b) corresponding spectral amplitudes** of the spintronic trilayer terahertz emitter as compared with the other three state-of-the-art terahertz emitters. The samples are excited with pump pulses of 10 fs duration and center wavelength of 800 nm, similar to the ones employed in this thesis. The figure is taken from [SJM+16].

addition, it exhibits an easy THz polarity flipping and polarization control through the applied STE magnetization. It is also pretty flexible in pump photon energy and excitation geometry. Furthermore, the construction of the spintronic emitter is low-cost and straightforward.

The goals for further improvement of the THz emission efficiency of the STE and a better understanding of the resulting spin dynamics are driving many research activities [PB20], [FQW+21].

2.3 THz detection: electro-optic sampling

The detection method used is based on a time-domain electro-optic sampling (EOS) pump-probe system. Electro-optic sampling is a pulse detection technique that employs the Pockels effect, also called linear electro-optic effect

[Boy20]. A significant advantage is that one can simultaneously determine the amplitude of the THz electric field and its phase with high accuracy. The working principle is demonstrated in Fig. 2.5.

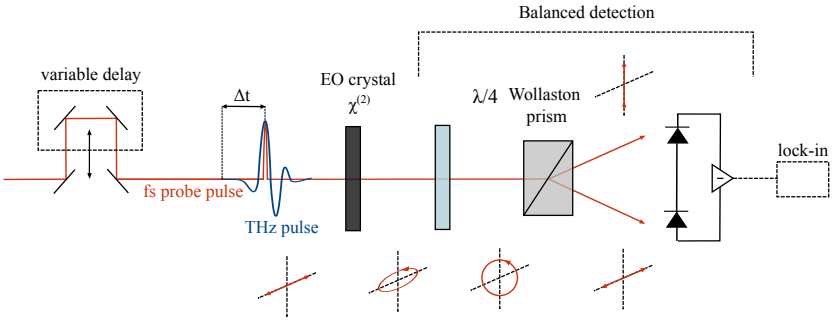

Figure 2.5: Electro-optic sampling and balanced detection of a THz waveform. The femtosecond optical probe pulse and the THz pulse propagate collinearly through the $\chi^{(2)}$ detection crystal. Due to the linear electro-optic effect, the presence of the THz field induces a transient birefringence in the crystal, proportional to the THz field amplitude, which converts the probe polarization from initially linear to elliptical. The induced ellipticity is measured with a balanced detection scheme, which is realized by a $\lambda/4$-wave plate, a Wollaston prism, i.e. polarizing beam splitter, and a pair of photodiodes. The photocurrent difference between the signals of the two photodiodes is proportional to the THz field amplitude at the position of the probe pulse, i.e., at a given time delay Δt. By moving the variable delay stage, the complete THz waveform can be scanned. Redesinged from [ZTR+13].

Pockels effect. It describes the instantaneous birefringence induced in an optical medium by an applied electric field (for instance, the THz pulse). It is a linear second-order $\chi^{(2)}$-effect, and hence it occurs only in media with broken inversion symmetry [Boy20].

The detection medium used in this work is a ZnTe(110) crystal (thickness of 300 μm). The THz transient and the femtosecond optical probe pulse -originating from the same laser as the pump pulses used for the THz generation-, arrive at the detector with a variable delay Δt. In the presence of the THz electric field, which is linearly polarized, a transient birefringence is induced, causing a change in the refractive index along one axis of the crystal. The induced birefringence is proportional to the THz field. The co-propagating optical probe pulse -also linearly polarized- experiences this birefringence, and therefore its polarization changes to slightly elliptical, depending on the THz field strength [ZX10].

Balanced detection scheme. The resulting probe ellipticity is measured with a balanced detection configuration, which consists of a $\lambda/4$-wave plate, a Wollaston prism (polarizing beam splitter), and a pair of photodiodes [ZX10].

Without the presence of the THz field, the $\lambda/4$-wave plate converts the initial probe polarized light into circular. The following Wollaston prism splits the two orthogonal optical components and sends them to the photodiodes, resulting in two equally sized signals. Once the THz field is present, the induced probe ellipticity leads to an unbalance on the two photodiodes. The photocurrent difference between the two photodiodes, proportional to the induced probe ellipticity and to the time-varying THz field strength, is fed into a lock-in amplifier, which is used to enhance the signal-to-noise ratio. The time delay between the probe and THz pulse is mechanically controlled with a variable delay stage, and thus one can perform successive sampling of different parts of the THz waveform. The THz field amplitudes can be recovered by the measured lock-in signal S(t) of the THz pulses, since S(t) is the convolution of the THz electric field incident onto the detector with the response function of the detection crystal (ZnTe).

It is important to note for following discussions that both probe and THz beam are focused and aligned to spatially overlap inside the detection crystal (see Fig. 2.6). A precise alignment ensures that the two beams are

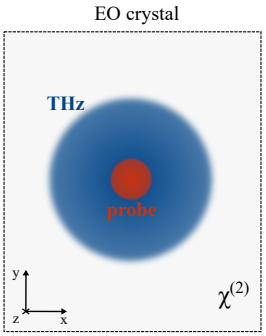

Figure 2.6: Spatial overlap between probe and THz focused beams inside the detection electro-optic crystal.

concentric. The focused probe beam size is much smaller than the THz beam, and a 'point'-probe can be assumed. For further understanding of the parameters that influence electro-optic sampling measurements one can find more detailed discussion on the work of Tomasino *et al.* [TPS+13] and Faure *et al.* [FTKL04].

Chapter 3

Curved-wavefront excitation geometry

From the initial excitation geometry of the STE employed for THz-STM measurements, several unwanted effects which limit the THz emission and propagation efficiency occur. For the plan of an optimized excitation geometry, which is the main goal of this thesis, it is first useful to disentangle all those effects. For that purpose measurements and simulations are performed. In this chapter, the results of this work are presented and discussed. First, in Section 3.1 the original experimental setup is described. In Section 3.2 the arising unwanted effects are separately presented and evaluated. Last, Section 3.3 recapitulates all the conclusions drawn in the previous section and provides design considerations for an optimized experimental setup.

3.1 Experimental setup

The STE is excited under normal incidence with near-infrared (NIR) femtosecond laser pulses (see Section 2.1) resulting in THz pulse generation. Figure 3.1 shows the experimental setup. The NIR pump beam is focused and recollimated by a pair of 90^o off-axis parabolic mirrors, creating a curved-wavefront excitation geometry once the STE is placed outside of the focus. The STE position along the propagation axis of the focused NIR pump beam can be altered by a translation stage, giving the flexibility to vary the excitation spot size and fluence incident to the emitter. The STE magnetization is controlled by a permanent magnet (M). The THz pulses can either be guided to the implemented electro-optic sampling for the detection or into the ultra-high vacuum champer for THz-STM measurements. The parabolic

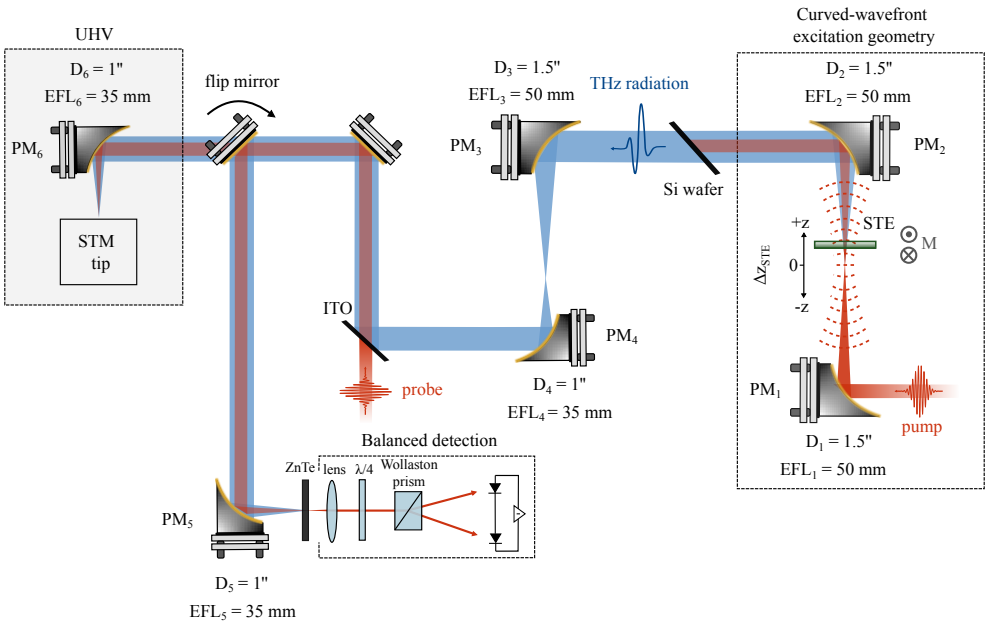

Figure 3.1: Curved-wavefront excitation geometry. The near-infrared femtosecond pulse (pump) is focused and recollimated by the first pair of 90^o off-axis parabolic mirrors. Along the propagation axis of the focused pump beam, the STE is placed in a translation stage. This gives the flexibility to move the emitter back and forth (Δz_{STE}), either to the convergent or divergent side of the beam, varying the excitation spot size and fluence incident onto the emitter. The STE magnetization is controlled by a permanent magnet (M). After the generation of THz radiation and the recollimation of the co-propagating beams, the remaining pump light is blocked by a Si wafer mounted near Brewster angle for maximum THz transmission. The next pair of 90^o off-axis parabolic mirrors, which comprises a telescope, decreases the THz beam size to match the parabolic mirror in the STM platform. On the indium-tin-oxide (ITO) coated glass, a near-infrared femtosecond pulse (probe) is collinearly overlapped to the THz beam path. The co-propagating beams are directed by the two plane mirrors onto the last 90^o off-axis parabolic mirror, where they are finally focused into the electro optic-crystal (ZnTe). The optical probe samples the THz pulse into the detection crystal, and eventually, the optical elements for the balanced detection follow (see Section 2.3). Alternatively, the flip plane mirror can be removed and the THz pulse can be lead to the ultrahigh vacuum chamber (UHV) where it will be focused onto the STM tip by an off-axis parabolic mirror integrated on the STM platform.

mirror used for focusing the beam onto the EO crystal is restricted by the STM geometry. Thus, it is chosen to be identical to the one integrated into the STM platform (35 mm effective focal length, 1-inch diameter). All the mirrors used are gold-coated. The experimental setup is enclosed, enabling nitrogen purging. Therefore, all measurements can be conducted in a dry nitrogen environment to avoid the absorption of terahertz radiation by the water molecules of the atmosphere [SSGG13].

The range of the available excitation NIR pump spot sizes can be seen in Fig. 3.2. The beam is measured with a CMOS board camera, and then two cuts along vertical and horizontal direction are performed.

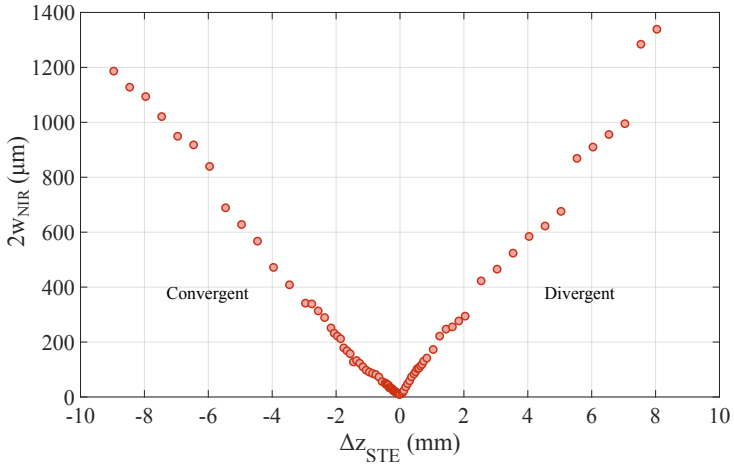

Figure 3.2: NIR pump beam diameter $(1/e^2)$ **versus** Δz_{STE}**.** The beam diameter value of each point, presented in this graph, is the average of the horizontal and vertical value.

Under these excitation conditions, several effects limit the THz emission and propagation efficiency. Those effects are discussed in detail in the following section.

3.2 THz emission and propagation efficiency

In combination with the employed laser parameters, the described experimental setup gives rise to several unwanted effects, which reduce the THz emission and propagation efficiency, altering the THz electric field amplitude, phase, and bandwidth measured in the EO crystal or the STM. An

attempt to disentangle those effects through measurements and simulations is presented in this section.

3.2.1 Ablation of the spintronic THz emitter

The spintronic THz emitter consists of thin films evaporated on some transparent substrate such as sapphire, as in our case. When placed close or inside the NIR focus and excited with high pump powers, the employed ultrashort laser pulses can easily ablate it and remove deposited STE material, leading to permanent damage. The ablation is a single-pulse event, and it is not determined by average quantities such as the pump power. Particularly, it depends on the pump pulses peak intensity, which is given by the formula

$$I_{peak} = \frac{E_p}{\tau A} \tag{3.1}$$

where E_p is the pump pulse energy, τ is the pulse duration, and A is the pump beam area.

Thus, since we employ few-femtosecond laser pulses with microjoule pump pulse energies, ablation easily occurs in small excitation beam sizes. It is an irreversible effect and defines a hard threshold of what pump beam size can be used at the given pulse energy and duration. From previous measurements, after observed permanent damage of the STE, the ablation limit is roughly estimated around ∼300 μm, when operating with full power (@ 4 μJ, 10 fs, 2 mJ/cm^2).

3.2.2 Saturation of THz emission efficiency

Following the excitation of the STE, based on Ohm's law, the amplitude of the emitted THz field E_{THz} will scale linear with the induced charge current density j_c, hence with the number of the excited electrons per volume [KBM+13], [SJM+16]. In turn, the induced current density will scale linearly with the laser average intensity I_{NIR} [DWHD06], and thus one can write

$$E_{THz} \propto j_c \propto I_{NIR} \propto \frac{P_{NIR}}{\pi w_{NIR}^2} \tag{3.2}$$

where P_{NIR} is the laser average power and w_{NIR} is the NIR pump beam radius.

Based on the above formula, the THz field is expected to scale linearly with the pump power. However, opposite to Eq. 3.2, a sublinear scaling with power can also occur. Saturation of the THz field amplitudes at high energies (or high pump powers) is observed, and it is more severe at small pump spot sizes. This trend is assigned to thermal heating effects inside the spintronic emitter. Since the STE consists of thin films and absorbs a significant part of the incident power, it is sensitive to heat. Operating close to the NIR focus, hence exciting the STE with small pump spot sizes, given the employed laser parameters, thermal heating can occur. It is important to emphasize that both static and transient heating may play a role in the observed saturation. The static heating is associated with the actual STE temperature and depends on average quantities, such as the average pump power. On the other hand, transient heating is associated with the heating of the electronic subsystem on ultrafast time scales and depends on single-pulse properties such as the energy density (fluence). Thermal heating mainly exhibits itself as a reversible and continuous effect, but it can also lead to permanent damage of the emitter. However, in contrast with ablation, thermal heating effects, at our pulse parameters, do not define a hard threshold of what pump spot size can be used. Ablation will dominate permanent damage before permanent damage due to heat occurs.

Measurements are performed to define the threshold for the excitation spot size above which the saturation effects are less prominent. In order to test how the THz signal scales with the pump power for different pump spot sizes, the STE is moved and excited in different positions along the propagation axis of the focused NIR beam. For each case, THz waveforms are measured with EOS detection (see Section 2.3) after excitation with high and low laser pump powers. The different power values influence mainly the amplitude of the signal and not the waveform shape. A typical THz waveform measurement is shown in Fig. 3.3. The measured electro-optic signal S(t) is linearly proportional to the THz electric field E_{det}(t) incident on the detector. More accurately, S(t) is the convolution of the E_{det}(t) with the response function of the detection crystal (ZnTe), and one can recover the THz field from the electro-optic signal. However, it is not necessary for the moment since only power scaling is examined.

After ensuring that the waveforms do not change and the waveform peaks

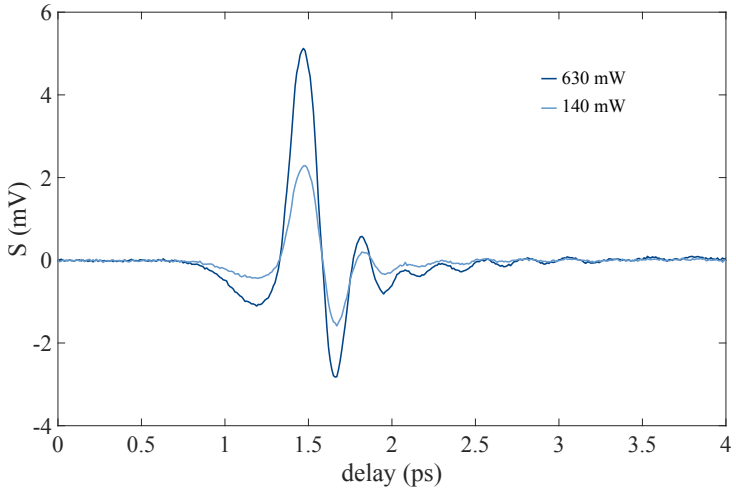

Figure 3.3: THz waveforms. THz waveforms measured at the same Δz_{STE} position in the convergent side of the NIR pump beam, at 0.5MH repetition rate, with high and low power. The different power values influenced just the THz amplitude and not the waveform shape.

do not shift with power, operating at the specific delay where the peaks appear, power scans are performed, and the peak THz signals are recorded. Note that ablation and white light generation in the sapphire substrate prevent using high pump powers at distances very close to the NIR focus. The nonlinearities which cause the white light in the sapphire substrate are not wanted as they can result in strong temporal and spatial distortions of the NIR pump pulse. In this regard, since the temporal shape of the excitation pulse will not be necessarily the same in high and low power regimes, the THz waveform shape could be affected. The pump power is controlled by two neutral density filters (ND) linearly varying in optical density. The filters are integrated into the pump beam path on a motorized stage. Also, a chopper wheel chops the THz generation beam for increasing the signal-to-noise ratio with lock-in detection (modulation frequency 607Hz). Fig. 3.4 depicts the peak THz amplitude versus NIR pump pulse energy for four different STE positions Δz_{STE}, i.e., for four different pump spot sizes, measured at the convergent side of the beam operating at 0.5 MHz repetition rate. The NIR pump beam diameter $2w_{NIR}$ for each position is extracted from the data of Fig. 3.2. Each curve is fitted with the function

$$f(x) = Ax^n \tag{3.3}$$

The results demonstrate that, especially for the distances closer to the NIR

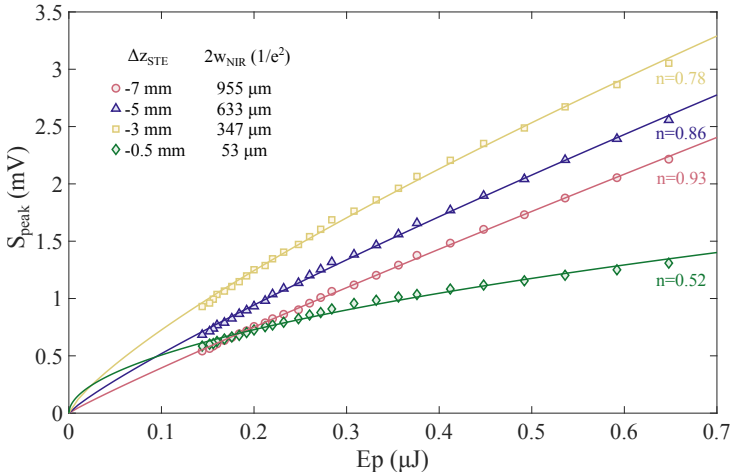

Figure 3.4: Peak THz amplitude $S(t)$ versus NIR pump pulse energy E_p measured at four different STE positions Δz_{STE}, at the convergent side of the beam. The THz amplitude scales sublinearly with the pump pulse energy (or power) due to the thermal effects on the STE. The lines are sublinear fits to the experimental data. The saturating effect becomes less prominent with increasing excitation spot size, and the THz field scales more linearly with the pump pulse energy. That is also indicated by the fitting coefficient n, which gradually approaches the value of one for larger pump spot sizes.

focus and, thus, smaller pump spot sizes, the THz field strength scales sublinearly with the pump pulse energy (or power). Moving to larger pump spot sizes, a more linear scaling gradually occurs. That is also clearly indicated from the fitting parameter n, which gradually approaches the value of one for larger pump spot sizes. Fig. 3.5 shows how the fitting coefficient scales with the pump beam diameter.

We assigned this observation to thermal heating effects inside the STE. In the current measurements, by varying the spot size, it is impossible to distinguish whether the saturation occurs due to 'average' heating or single-pulse effects since both the power density and the energy density are simultaneously increased. To disentangle those two effects on the THz emission efficiency, measurements that vary the repetition rate are required. Recent results on the work of Vogel *et al.* [VOM+21] show that the saturation of the field is determined more by the transient heating, thus by single-pulse properties such as the energy density (fluence).

To conclude, in the current setup and at the given laser parameters, the STE has to be excited away from the NIR focus to prevent saturation effects

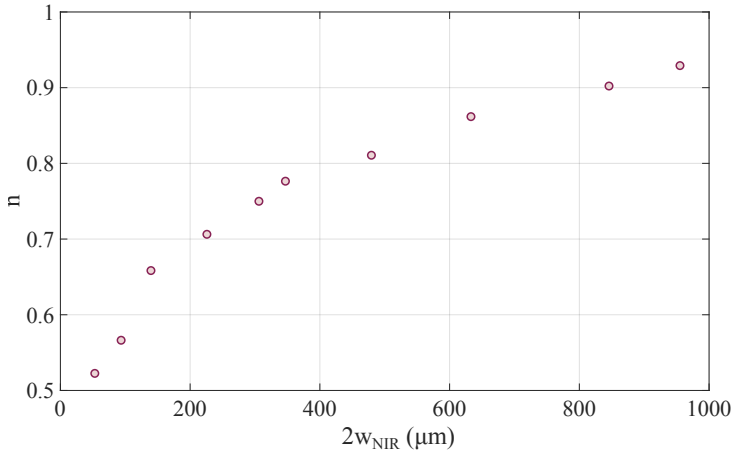

Figure 3.5: Fitting coefficient n versus NIR pump beam diameter. With increasing pump beam diameter the fitting coefficient n aproaches the value of one, resulting in a more linear depedence of the THz electric field with the pump pulse energy.

of the THz emission efficiency. However, it is also important to note that the overall THz amplitude is reduced for larger pump spot sizes. Such behavior is expected, as the THz field scales with fluence, i.e., reduces quadratically with the pump beam radius (see Eq. 3.2). This reduction might also be due to decreased collection efficiency, as the emitter is moved out of the focal point of the PM_2. That effect is examined in detail in one of the following subsections.

3.2.3 THz Emission from subwavelength volumes

For the generation of THz radiation, near-infrared light is used. Between those two regions of the electromagnetic spectrum, there is considerable variation in wavelengths. With the THz wavelengths (300 μm to 3 μm) being orders of magnitude longer than the wavelengths of the optical regime (centered around 800 nm), based on the diffraction limit, the optical field can be focused into much smaller spot sizes than the THz field. Therefore, using NIR pump spot sizes that are much smaller than the THz wavelengths, a THz source of radiation with a smaller spatial extent than is generally allowed by the diffraction limit can be generated. That results in evanescence waves on the emitter's surface (see Subsection 1.1.1). The near-field evanescence components do not carry electromagnetic energy to the far-field,

decreasing the THz emission efficiency, thus reducing the emitted THz field amplitudes.

For a quantitative understanding of the THz generation from subwavelength volumes, numerical simulations are performed. Initially, both NIR and THz radiation are modeled as Gaussian beams (see Section 1.2), and in a second step, the subwavelength model is applied to the THz parameters. First, a focused NIR pump beam of 5 μm beam waist, infinity radius of curvature in the focus position, and a wavelength of 800 nm is assumed. The NIR beam waist is chosen to fit the experimental value (see Fig. 3.2). Then, the radius $w_{NIR}(z)$ and the radius of curvature $R_{NIR}(z)$ of the NIR beam along a defined propagation axis z are calculated using the Eq. 1.13 and Eq. 1.15, respectively. Furthermore, the THz spectrum of interest is introduced, ranging from 1 THz to 30 THz. Additionally, an artificial Gaussian spectral weighting $A_{in}(\omega)$ on the different frequency components is implemented:

$$A_{in}(\omega) = \frac{1}{\sigma\sqrt{2\pi}} e^{-\frac{1}{2}(\frac{\frac{\omega}{2\pi}-\mu}{\sigma})^2} \tag{3.4}$$

centred at $\mu = 3$ THz, and with $FWHM = 2\sqrt{2ln2}\,\sigma = 30$ THz. Those values are chosen based on the spectral bandwidth of the spintronic emitter. As in the experimental setup, the THz generation can be done at any position along the z-axis. This implies that any pair of the calculated values $w_{NIR}(z)$ and $R_{NIR}(z)$ at a specific position along z can be used to generate the initial THz beam radius and radius of curvature. For that, a variable parameter Δz_{STE} is inserted and represents the position along the propagation axis where the THz generation happens. At z=Δz_{STE}, it is assumed that the radius and the wavefront curvature of the NIR pump beam are imprinted on the THz field. Practically this means that the initial frequency-dependent complex radius of curvature q_{THz} of the THz beam can be calculated, utilizing the Eq. 1.18, where the values for the radius and the wavefront radius of curvature of the THz beam are substituted by those of the NIR beam (w_{NIR}, R_{NIR}) at Δz_{STE} correspondingly. Moreover, for the wavelengths, the THz spectrum of interest is inserted.

Finally, the spectral weighting $A_{in}(\omega)$- which corresponds to the initial electric field strength of the THz spectrum-, the calculated frequency-dependent complex radius of curvature q_{THz} of the THz beam, and the THz spectrum of interest, are used as an input to the function which models the subwavelength emission. Note that the numerical aperture (NA) of the collecting parabolic mirror PM_2 (see Fig. 3.1), which follows the THz gen-

eration, is used as an input too. For a detailed description of the utilized subwavelength emission model, look at the work of Seifert *et al.* [STG+18] (see Supplementary data). The output of this calculation provides the electric field amplitude $A_{subwl}(\omega)$ on the emitter's surface. The resulting value of the calculated THz electric field reflects the subwavelength emission and no propagation effects. Therefore, the transfer function of the subwavelength emission can be calculated as:

$$H_{subwl}(\omega) = \frac{A_{subwl}(\omega)}{A_{in}(\omega)} \tag{3.5}$$

considering $A_{in}(\omega)$ as the input and $A_{subwl}(\omega)$ the output of the model.

Fig. 3.6 shows the calculated electric field amplitude $A_{subwl}(\omega)$ on the emitter's surfaces plotted versus the THz frequencies for several excitation positions Δz_{STE}, thus pump spot sizes. For each case, the used simulated value of the NIR pump beam diameter $2w_{NIR}$ $(1/e^2)$ is depicted. The dashed line in the graph is the input artificial Gaussian spectrum $A_{in}(\omega)$, which corresponds to the electric field strength of the THz spectrum before the subwavelength model is applied. The result demonstrates that moving closer

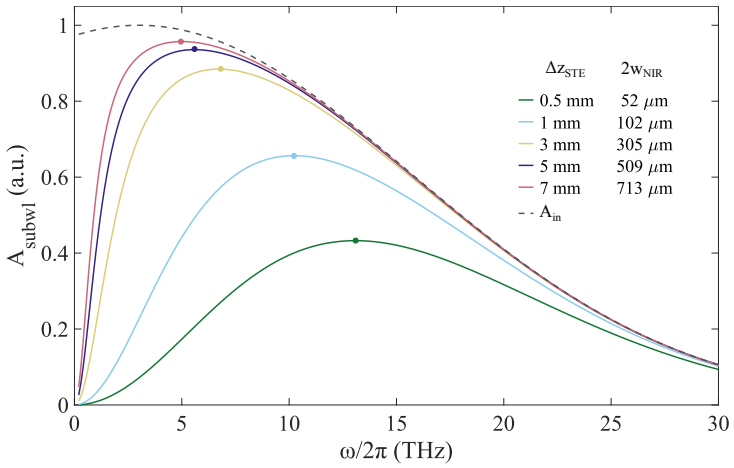

Figure 3.6: A_{subwl} vs THz spectrum. The dashed line is the artificial spectral weighting on the different frequency components. After applying the subwavelength emission model, for different excitation positions (Δz_{STE}), and thus for different excitation spot sizes ($2w_{NIR}$), the resulting THz electric field amplitude A_{subwl} is calculated and plotted versus the THz spectrum. For distances closer to the NIR focus, and thus, smaller pump beam sizes, the emission is suppressed, and blue shifted.

to the NIR focus, thus using smaller excitation spot sizes, the overall THz electric field amplitude is reduced and blue shifted.

To understand better how each THz frequency component is suppressed, it is useful to look at the transfer function of the subwavelength emission $H_{subwl}(\omega)$. Fig. 3.7 depicts the H_{subwl} plotted versus the THz spectrum for different excitation positions (Δz_{STE}). As expected, moving closer to the

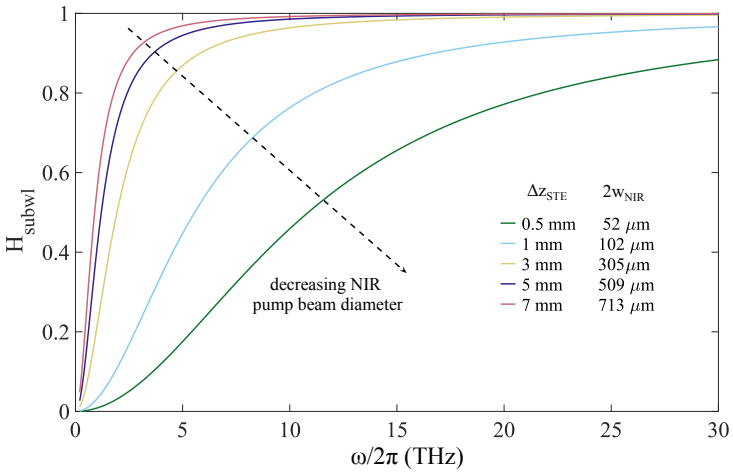

Figure 3.7: Transfer function of subwavelength emission versus THz spectrum. For the smaller NIR pump spot sizes, the low THz frequencies are suppressed stronger than the high ones. The subwavelength emission works as a high pass filter.

NIR focus, thus using smaller excitation spot sizes, the low THz frequencies are suppressed stronger. The subwavelength emission works as a high pass filter. Considering a THz-frequency spectrum range from 1 THz to 30 THz, this is translated to approximately a wavelength range from 300 μm to 10 μm. Therefore, the low frequencies -having bigger wavelengths- are more sensitive to the subwavelength volumes when the pump spot size gets smaller.

To conclude, the mismatch between the optical and THz wavelengths can lead to THz radiation from subwavelength volumes, resulting in the inefficient coupling of the generated evanescence near-field to the far-field, reducing the emitted THz field amplitudes. That suggests that excitation spot sizes larger than the wavelengths of all THz frequency components should be used to avoid this effect and improve the THz emission and propagation efficiency. Note that this option in our case is possible since the employed laser source provides enough power. However, a tight focus might be needed for low pulse energy laser systems to achieve enough fluence, compromising

subwavelength emission.

3.2.4 Chromatic aberrations

Considering the above-listed unwanted effects, it is clear that many factors can influence the efficient excitation of the STE close or in the focus position of the NIR pump beam. On the other hand, when placing the emitter further away, out of the NIR focus to handle better those effects, the curved-wavefront excitation geometry gives rise to strong frequency-dependent THz propagation, i.e., strong chromatic aberrations. That results in a decreased collection efficiency of the THz frequency components, reducing the THz field amplitudes reaching the EO crystal or the STM tip.

The collecting parabolic mirror PM_2, which comes after the excitation of the STE, is adjusted to perfectly re-collimate the NIR pump beam (see Fig. 3.1). Thus, its focal point lies at z=0. Once the STE is placed anywhere else than the z=0 ($\Delta z_{STE} \neq 0$), all THz frequencies are moved out of the focal plane, and their focus position does not coincide anymore with the NIR pump focus. The focus position of the emitted THz frequencies depends on the pump spot size and NIR wavefront radius of curvature with which the STE is excited. Depending on whether the STE is excited on the NIR beam's convergent or divergent side, the THz focus positions are located after or before the STE, respectively. Therefore, the parabolic mirror cannot collect the THz frequencies uniformly and effectively, making the re-focusing into the EO crystal or the STM tip inefficient. Since the emitted THz spectrum is ultra-broad, the THz focus positions can vary strongly depending on the frequency; thus, each frequency component behaves considerably differently inside the optical setup.

Numerical simulations are performed to visualize and understand better the resulting propagation of the THz spectrum along the z-axis. Both NIR and THz radiation are modeled as Gaussian beams (see Section 1.2). First, the calculation of the NIR beam (radius $w_{NIR}(z)$ and radius of curvature $R_{NIR}(z)$) along a defined propagation axis z and of the initial frequency-dependent complex radius of curvature q_{THz} of the THz beam are done as described in Section 3.2.3. Note that also, as before, any pair of the calculated NIR pump beam parameters can be used to initiate the THz generation, using the variable parameter Δz_{STE}. Then, the ABCD matrix formalism (see Section 1.3) is applied, using the calculated complex q_{THz}

parameter as an input. In particular, the transfer matrix for propagation in free space (Eq. 1.22) is utilized, and each THz frequency is independently propagated through the air. From the evaluated $q_{THz}(z,\omega)$ parameter along the propagation axis, the beam size and radius of curvature for each THz component along z is extracted. Some plotted results follow.

Assuming that the STE is excited in the convergent side of the NIR pump beam, 3 mm behind the focus ($\Delta z_{STE} = -3$ mm), Fig. 3.8 shows how the beam radius $w(z)$ of five selected THz frequencies evolves along the propagation axis z. The sketch above the figure is a visual description of the plot. The chromatic aberrations become apparent. Once the STE is placed

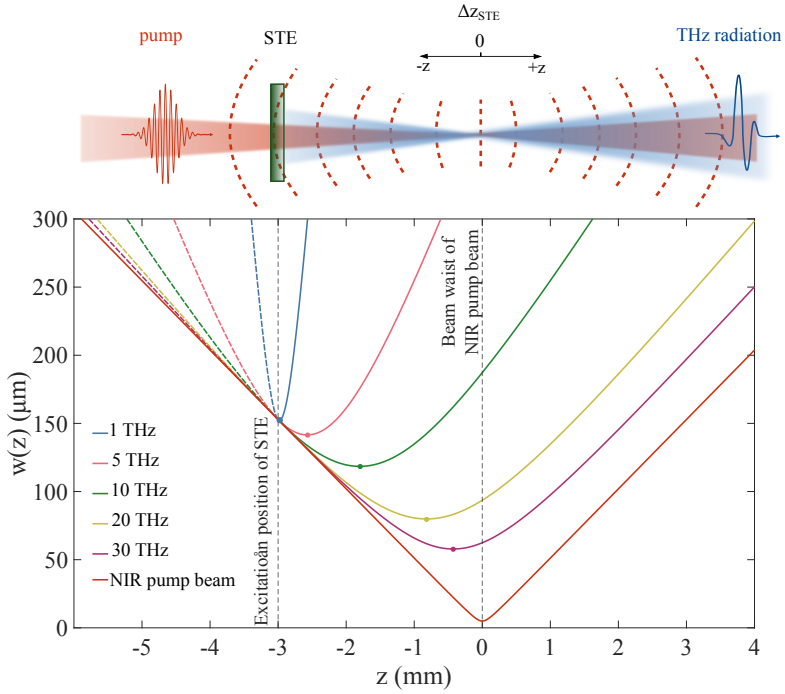

Figure 3.8: Frequency-dependent THz focus after the STE. It is assumed that the STE is excited in the convergent side of the NIR pump beam, 3 mm away from the focus. The resulting numerically calculated beam radius $w(z)$ of five selected THz frequencies is plotted versus the propagation axis z. The THz focus (colorful dots) is located after the STE and shifts as a function of frequency. The solid red line is the NIR pump beam. The dash part of the curves indicates the back-propagating THz beam.

before the focal plane of the NIR pump beam, a THz focus after the emitter is generated. The focus shifts several mm as a function of frequency. For the setup, this implies that each THz frequency has a different focal plane;

therefore, the collecting parabolic mirror PM_2 can not collect all frequencies in the same way. The low frequencies exhibit high divergences. In addition, their focal plane is strongly shifted compared to the NIR focus, based on which the collecting parabolic mirror is aligned. Therefore, low frequencies can not be collected so efficiently. Consequently, one could say that the overall behavior works as a high pass filter, as the high frequencies will be collected more effectively, leading to a better propagation inside the optical setup and finally better imaging in the EO crystal or the STM tip.

In Fig. 3.9, a similar result occurs when assuming that the STE is excited in the divergent side of the NIR pump beam, 3 mm after the focus ($\Delta z_{STE} =$ 3 mm). The only difference, in this case, is that the frequency-dependent

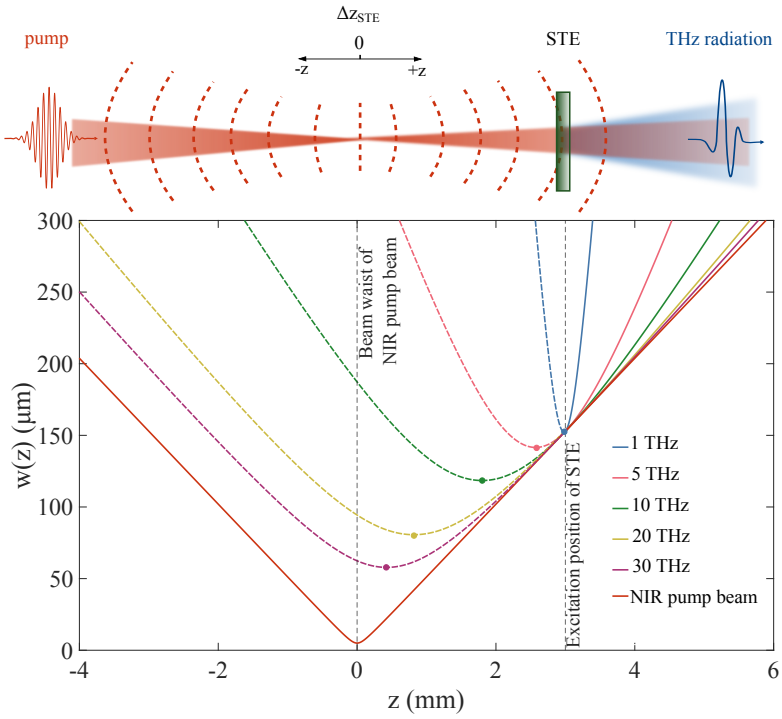

Figure 3.9: Frequency-dependent THz focus before the STE. It is assumed that the STE is excited in the divergent side of the NIR pump beam, 3 mm away from the focus. The resulting numerically calculated beam radius $w(z)$ of five selected THz frequencies is plotted versus the propagation axis z. The THz focus (colorful dots) is located before the STE and shifts as a function of frequency. The solid red line is the focused NIR pump beam. The dash part of the curves indicates the back-propagating THz beam.

THz focus is located before the STE.

To achieve THz-frequency independent collimation and re-focusing requires that the THz focus is located in the focal plane of the collecting parabolic mirror PM_2 for all THz frequencies. That is possible just in case the STE is excited in the focal plane of the NIR pump beam ($\Delta z_{STE} = 0$ mm). Fig. 3.10 recapitulates the above results and demonstrates how the THz focus position changes along the propagation axis z as a function of frequency for three different STE excitation positions.

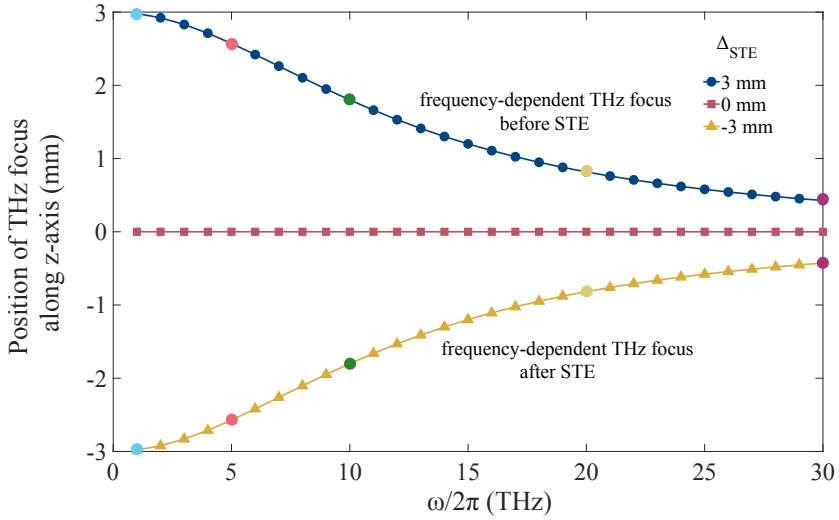

Figure 3.10: THz focus position as a function of the THz frequency. Once the STE is placed out of the NIR focal plane ($\Delta z_{STE} \neq 0$) mm, the THz focus shifts as a function of frequency. A frequency-dependent THz focus located after the STE occurs in the case in which the emitter is excited in the convergent side of the pump beam ($\Delta z_{STE} = -3$ mm), while a frequency-dependent THz focus located before the STE occurs when the emitter is excited in the divergent side of the beam ($\Delta z_{STE} = 3$ mm). However, placing the STE in the NIR focal plane ($\Delta z_{STE} = 0$ mm), the THz focus is located in z=0 for all THz frequencies.

To conclude, the position of the THz focus is determined by the NIR spot size, the NIR wavefront curvature, and the THz-frequency. In the current setup, the STE has to be excited in the NIR pump focus to avoid chromatic aberrations and improve the THz collection efficiency. However, as it has been demonstrated in the above discussion, several effects prevent this option. Therefore, a plane wave excitation geometry, that is, a weakly focused or collimated NIR pump beam, is needed for reducing the chromatic aberrations and achieving higher THz field amplitudes.

3.3 Remarks and design considerations for an optimized experimental setup

For a clear motivation and directions for an optimized excitation geometry, it is helpful to mention once again what is the goal of this work and recapitulate the main points drawn in the previous section. We aim to have a high THz electric field at the STM tip. First, for meeting that goal, high excitation fluence is needed for achieving high emitted THz powers. Furthermore, an efficient THz propagation is necessary for tight focusing onto the STM tip and thus attaining higher focused THz fields.

In the described experimental geometry, due to the tightly focused NIR pump beam used for the excitation, combined with the laser parameters of high repetition rate and large average power, many simultaneous effects occur that reduce the THz emission and propagation efficiency. Placing the emitter inside or close to the NIR focus for excitation with small spot sizes and, thus, high fluence, ablation can irreversibly damage the spintronic emitter with increasing power. Furthermore, in this regime, saturation effects and emission from subwavelength volumes drastically reduce the emission efficiency of the STE, resulting in smaller THz field amplitudes. To excite with larger spot sizes and thus handle better those effects, the emitter is placed further away from the focus position. In turn, this gives rise to strong chromatic aberrations, leading to inefficient propagation and inefficient re-focusing onto the STM tip, drastically reducing the achievable THz amplitudes.

It is thus evident that a new excitation geometry is needed. A critical fluence should not be exceeded to avoid ablation and saturation effects. The ideal pump spot size also depends on the available pump power. For using large pump powers, larger spot sizes are required to stay below the limiting fluence threshold. However, given limited average power, too large pump beams can also lead to decreased THz amplitudes, as the THz field is expected to scale with fluence, i.e., to reduce quadratically with the pump beam radius. Therefore, an optimum spot size must be found, which will compromise those effects. For this purpose, the new excitation geometry enables the variation of the pump spot size, and thus, the THz field dependence on it can be investigated. At the same time, it is essential to excite the spintronic emitter with a collimated or weakly focused pump beam to reduce the chromatic aberrations and achieve better THz propagation through the optical system. Note that even if all the above parameters are optimized, we also need to re-focus the THz beam very tightly onto the STM tip or

EO crystal to enhance the THz field strength. That means a large beam diameter is needed onto the STM/EOS re-focusing parabolic mirror. In this regard, important design consideration for the new setup is that THz beam size has to be expanded to match the size of the re-focusing parabolic mirror (1-inch mirror diameter). For this purpose, an expansion telescope of the THz beam is built in the new geometry.

Chapter 4

Plane-wavefront excitation geometry

This chapter presents a plane-wavefront THz excitation geometry, constructed during the work of this thesis based on the acquired knowledge described previously (see Chapter 3). The new geometry enables the use of different NIR pump beam sizes. Thus, optimum excitation conditions for the STE, which will provide higher THz fields amplitudes, can be investigated. First, Section 4.1 demonstrates the experimental setup. Numerical simulations of THz propagation through optical systems were necessary to design a new setup and interpret experimental results. Taking into consideration all limitations regarding the pump spot size and the optical geometry described in Chapter 3, different excitation geometries are numerically tested. The following described experimental setup is decided to be the most efficient among all available ideas. In Section 4.2 the model and the outcome of the numerical simulations are discussed. Last, Sections 4.3 and 4.4 contains the experimental details and the results of the measurements performed in the particular geometry.

4.1 Experimental setup

The STE is excited under normal incidence, with a collimated beam of near-infrared (NIR) femtosecond laser pulses (see Section 2.1). The excitation geometry enables the use of three different pump spot sizes. Figure 3.1 demonstrates the experimental setup.

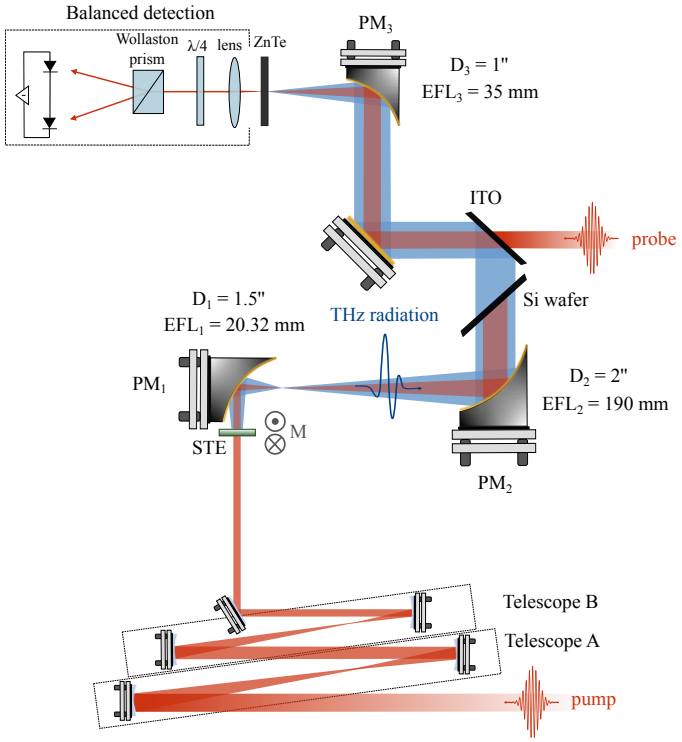

Figure 4.1: Optimized plane-wavefront excitation geometry. The STE is excited with a collimated beam of near-infrared (NIR) femtosecond laser pulses (pump). The NIR pump beam diameter is controlled by two successive telescopes realized by pairs of concave mirrors (Telescope A and B), allowing the use of three different pump spot sizes. Exiting Telescope B, a plane mirror directs the NIR pump beam onto the STE. The STE, placed in a distance equal to the effective focal length of the collecting parabolic mirror (PM_1), is excited under normal incidence, leading to THz pulse radiation collinear with the NIR pump beam. The STE magnetization is controlled by a permanent magnet (M). The collecting 90^o off-axis parabolic mirror PM_1 together with the following 90^o off-axis parabolic mirror PM_2 comprise a third telescope, which expands the THz beam size. The remaining pump light is blocked by a Si wafer, mounted near Brewster angle for maximum THz transmission. On the indium-tin-oxide (ITO) coated glass, a near-infrared femtosecond pulse (probe) is collinearly overlapped to the THz beam path. A plane mirror directs the co-propagating beams onto the last 90^o off-axis parabolic mirror (PM_3), where they are finally focused into the electro optic-crystal (ZnTe). The optical probe samples the THz pulse into the detection crystal, and eventually, the optical elements for the balanced detection follow (see Section 2.3).

For the variation of the NIR pump beam diameter, two successive telescopes are constructed (Telescope A and B). The telescopes are designed to achieve a range of excitation spot sizes, which follow the limitations drawn in the previous chapter. Telescope A has a fixed ratio and is realized by a pair of silver-coated (Ag) concave mirrors. Telescope B has a variable ratio and can have three different configurations, using three different mirror pairs and always keeping the distance of the mirrors constant. Table 4.1 contains detailed information about the optical elements used for telescopes A and B, including for each configuration the resulting theoretical NIR pump beam diameter $2w_{NIR}$. Those values are calculated considering as an input of Telescope A the initial experimentally defined value of the laser output. The initial NIR pump beam is measured to have a diameter of (7.83 ± 0.02) mm ($1/e^2$). The measurement is conducted in the horizontal direction of the beam with the knife-edge method (see App. A). The second mirror of Telescope B is mounted on a linear stage to optimize the collimation of the outcome beam. After Telescope B, the NIR pump beam is directed by a

Telescope A		
Mirror pairs	Ratio	$2w_{NIR}$ $(1/e^2)$
Ag concave mirrors of (150+250 mm) EFL	1:1.67	4.7 mm
Telescope B		
Mirror pairs	Ratio	$2w_{NIR}$ $(1/e^2)$
Ag plane mirrors	1:1	4.7 mm
Ag concave mirrors of (100+200 mm) EFL	1:2	2.35 mm
Ag concave mirrors of (50+250 mm) EFL	1:5	0.94 mm

Table 4.1: Available configurations for Telescope A and B. Telescope A has a fixed ratio, reducing the NIR pump beam size by a factor of ∼1.67. With the successive Telescope B, there are three options. Either the resulting NIR pump beam size can be maintained by using a pair of plane mirrors, or it can be further reduced by a factor of 2 or 5, using two different pairs of concave mirrors. The NIR beam diameter values are theoretical calculations based on the telescope ratios and the experimentally defined initial NIR beam diameter (see Fig.A.2).

plane mirror onto the STE, which is placed at a distance equal to the effective focal length of the collecting parabolic mirror (PM_1). This distance was chosen as optimum for an efficient THz collection by the PM_1, after numerical simulations, which are discussed in the following section (see Section 4.2). The STE magnetization is controlled by a permanent magnet (M). The collecting 90^o off-axis parabolic mirror PM_1 together with the following 90^o off-axis parabolic mirror PM_2 form a third telescope, which expands the THz beam size by a factor of ∼9.35. The ratio of the expansion-telescope (PM_1 and PM_2) is chosen so that, ideally, the resulting THz beam diameter matches the diameter of the parabolic mirror integrated into the STM platform. This will enable tight re-focusing, and the strong confinement of the THz radiation will result in enhanced THz electric field amplitudes. The off-axis parabolic mirror PM_3 used for focusing the beams onto the EO crystal (ZnTe) is restricted by the STM geometry. Thus it is chosen to be identical to the one integrated into the STM platform (35 mm effective focal length, 1-inch diameter). The optical probe samples the THz pulses into the detection crystal, and eventually, the optical elements for the balanced detection follow (see Section 2.3). Since the precise alignment of the probe and THz beam focused onto the detection crystal is critical, note that the ZnTe is mounted on a linear stage. Moreover, that enables further optimization of the measured signals in relation to the crystal's position. Mirrors are preferred over lenses to avoid temporal distortion of the ultrashort pulses. All the mirrors used after the THz generation are gold-coated. The experimental setup is enclosed, enabling nitrogen purging. Therefore, all measurements can be conducted in a dry nitrogen environment to avoid the absorption of THz radiation by atmospheric water vapor [SSGG13].

4.2 Numerical simulation of THz propagation

Numerical simulations of THz propagation through the optical system described above provide physical insight into how the different THz frequency components behave along the propagation axis under excitation with different NIR pump spot sizes. Furthermore, through the code, the transfer function of propagation is calculated and used later on for purposes regarding the data analysis. In this section, after presenting the employed model, some results assuming theoretical values of the NIR pump beam size -inside the range of interest-, are demonstrated and discussed.

Both NIR and THz radiation are modeled as Gaussian beams (see Section 1.2). Firstly, a beam waist w_{NIR} and radius of curvature R_{NIR} of the NIR pump beam are defined. The radius of curvature R_{NIR} is set to infinity, given a plane-wavefront excitation. The pump beam waist selectively can be changed for testing different NIR spot sizes. The parameters (radius and effective focal length) of the three parabolic mirrors PM_1, PM_2 and PM_3 following the THz generation are inserted. In addition, the THz spectrum (ω) of interest is introduced, ranging from 1 THz to 30 THz. The model sets off with the generation of the initial THz beam parameters (radius and radius of curvature), calculating a starting frequency-dependent complex radius of curvature q_{THz}. For this purpose, it is assumed that the radius and the wavefront curvature of the NIR pump beam are imprinted on the THz field. In this regard, the Eq. 1.18 is used for the calculation, where the values for the radius and the wavefront radius of curvature of the THz beam are substituted by those of the NIR beam (w_{NIR}, R_{NIR}), correspondingly. Moreover, for the wavelengths, the THz spectrum of interest is inserted. Then, utilizing the ABCD matrix formalism (see Section 1.3), each THz frequency component is propagated independently inside the optical system, along a defined propagation axis z. The transfer matrix of the system (see Fig. 4.1) is constructed given the alternate sequence: propagation through air (see Eq. 1.22) and the parabolic mirrors(PM_1, PM_2, PM_3). The parabolic mirrors are modeled as lenses (see Eq. 1.24). This calculation yields the knowledge of $q_{THz}(z,\omega)$ parameter -from which the THz beam radius and radius of curvature can be extracted-, along the whole propagation axis, for all THz frequencies. Note that the Si-wafer and the ITO are neglected in the simulations, since they have no effect on the propagation characteristics of the THz beam. In parallel, the on-axis (x=y=0) THz field amplitude $A(z,\omega)$ of the spectrum along the propagation axis z is calculated by employing the Eq. 1.20 and the respective $q_{THz}(z,\omega)$ parameter. Therefore, the transfer function of propagation $H_{prop}(\omega)$, can be estimated by the relation:

$$H_{prop}(\omega) = \frac{A_{out}(\omega)}{A_{in}(\omega)} \tag{4.1}$$

where $A_{in} = 1$, is an implemented artificial flat spectrum, which corresponds to the initial electric field strength of the THz components, and $A_{out}(\omega)$ is the calculated on-axis THz field amplitude, at the position of the propagation axis which corresponds to the focal point of the last parabolic mirror (PM_3), i.e., the position where the EO crystal would be located.

Considering the optical system described in Section 4.1 and given the ex-

pected theoretical values of the NIR pump beam diameter of Table 4.1, the beam radius of the THz frequencies along the propagation axis is calculated and plotted for the three different cases. Figure 4.2 depicts the results, assuming the NIR pump beam diameter to be $2w_{NIR} = 4.7$mm. For simplicity, only selected frequency components are plotted.

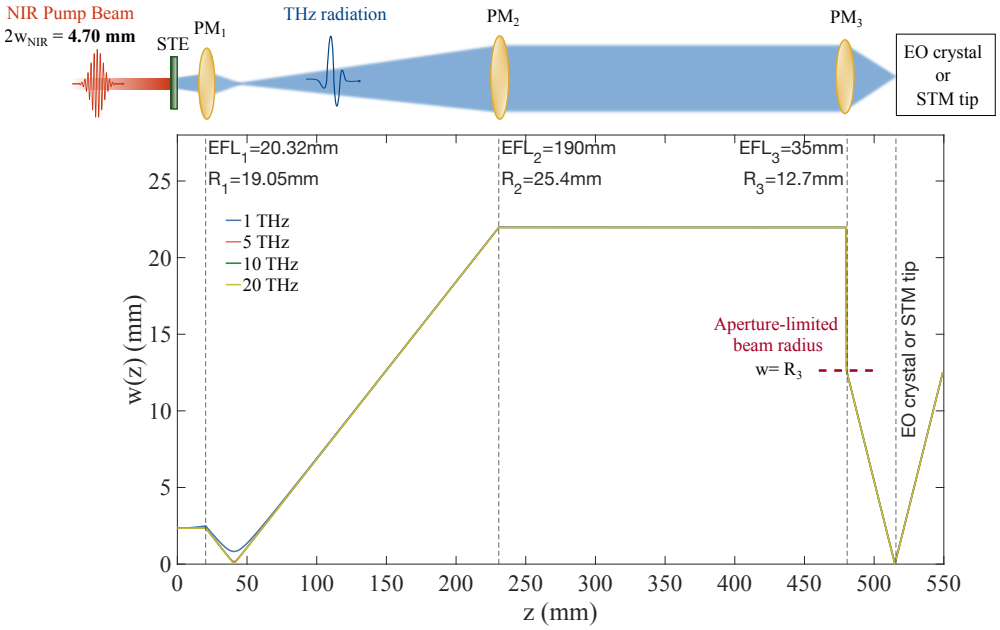

Figure 4.2: Assuming a NIR pump beam diameter of 4.70 mm, the beam radius w(z) for four selected THz frequencies along the propagation axis z is numericaly calculated and plotted. The sketch above the graph is a visual description of the THz generation and propagation through the simulated optical system. At the position of the last parabolic mirror PM_3 an aperture-limited beam radius is observed, and its value is defined by the size of the PM_3 (1-inch).

The sketch above the graph visually describes the THz generation and propagation through the simulated optical system. The position of each element drawn in the figure directly correlates to the positions along the propagation axis on the plot below them. The collimated NIR beam has a specific diameter and excites the STE under normal incidence. The STE is drawn to be at z=0. There, the assumption that the NIR beam parameters are imprinted on the THz field applies, and the model of the THz propagation is initiated. Then, the two parabolic mirrors (PM_1 and PM_2), which realise the telescope for enlarging the THz beam follows. Next, a propagation

distance of 250 mm is implemented, and it is defined by the position of the last parabolic mirror PM_3 used to focus the THz beam onto the EO crystal or STM tip. On the plot, the horizontal small dashed red line indicates the aperture of the last parabolic mirror PM_3. At this position, an immediate drop in the beam radius is observed. The size of the beam is limited by the size of the PM_3, which has a diameter of 1-inch. If $w > R_3$, the beam radius is set to be equal to the radius of the mirror.

Figure 4.3 depicts similar results, but assuming the NIR pump beam diameter to be $2w_{NIR} = 2.35$ mm, i.e., twice smaller than the previous value.

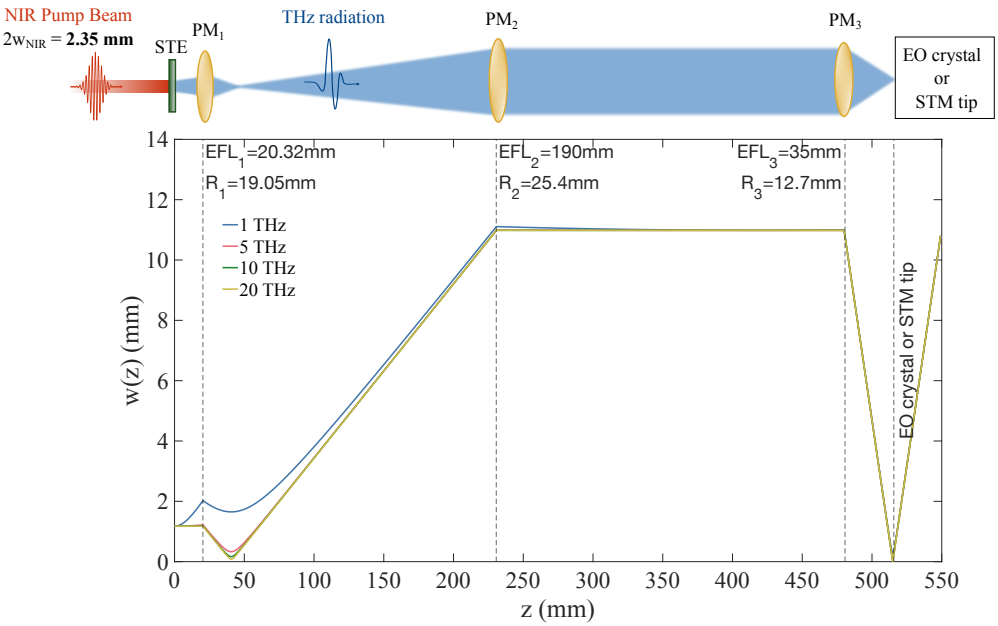

Figure 4.3: Assuming a NIR pump beam diameter of 2.35 mm, the beam radius w(z) for four selected THz frequencies along the propagation axis z is numerically calculated and plotted. The sketch above the graph is a visual description of the THz generation and propagation through the simulated optical system. For the low frequencies, a divergence occurs at the starting position. Although the collection, propagation, and re-focusing by the last parabolic mirror PM_3 seems efficient for all THz frequencies.

By reducing the excitation spot size, the resulting THz beam, especially for the low frequencies, becomes divergent. In this case, the aperture effect is not present. Entering the telescope with a smaller THz beam size than before, the resulting enlarged beam will also have a smaller size. Note the

different y-axis scaling compared to the previous graph (Fig. 4.2). The collection, propagation, and re-focusing for all THz frequencies look efficient.

Last, Figure 4.4 depicts similar results, but assuming the NIR pump beam diameter to be $2w_{NIR} = 0.94$ mm.

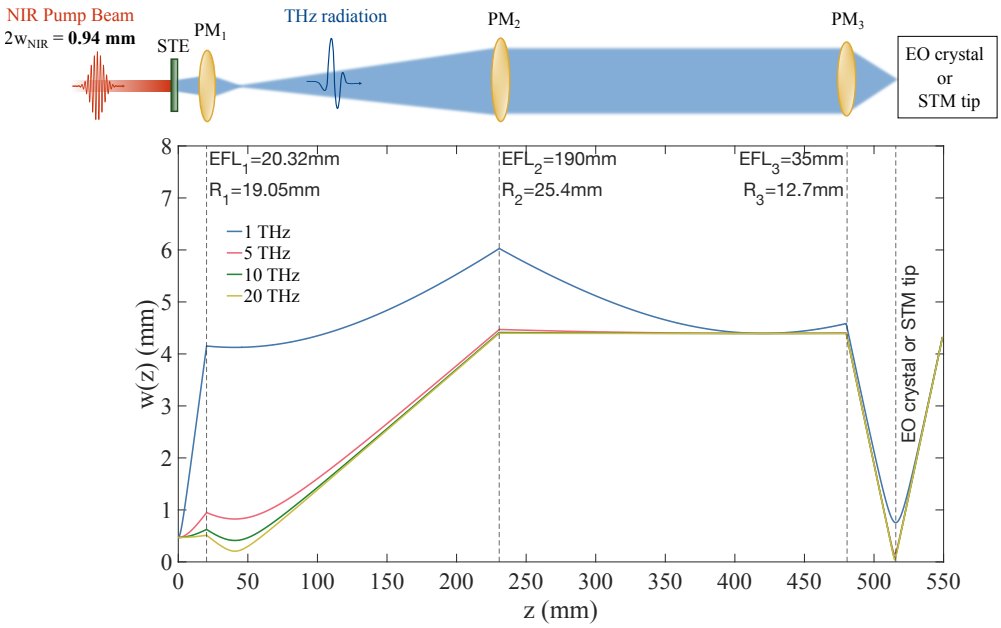

Figure 4.4: Assuming a NIR pump beam diameter of 0.94 mm, the beam radius w(z) for four selected THz frequencies along the propagation axis z is numerically calculated and plotted. The sketch above the graph is a visual description of the THz generation and propagation through the simulated optical system. The generated THz frequencies diverge pretty fast, leading to insufficient propagation through the optical system, and in the end, to less tight re-focusing onto the EO crystal or STM tip.

In this case, even higher THz frequencies diverge pretty fast. Therefore, especially for smaller excitation spot sizes, it is crucial that the STE is placed at a close distance with the collecting parabolic mirror PM_1. Looking at the case of 1 THz, it is obvious that its propagation through the optical setup becomes insufficient, leading to a less tight re-focusing on the EO crystal or STM tip, meaning in less enhanced THz field amplitudes.

To quantify all the above discussion, the transfer function of propagation $H_{prop}(\omega)$ is calculated for several NIR pump beam diameters $2w_{NIR}$ -inside the range of interest-, and plotted versus the THz frequency components.

Fig. 4.5 depicts the results.

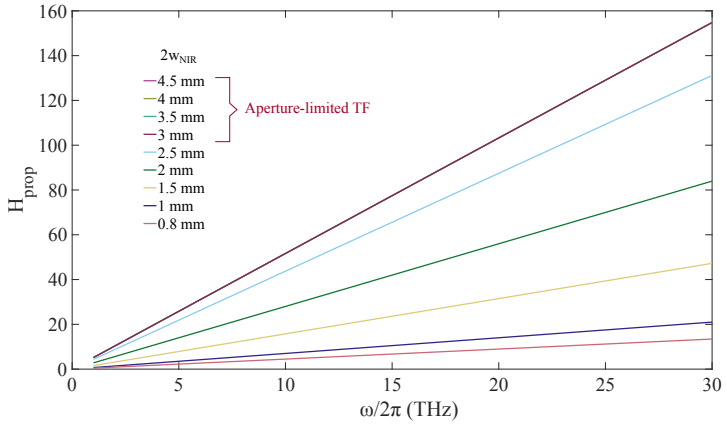

Figure 4.5: The transfer function of propagation H_{prop} is numerically calculated and plotted versus the THz frequency spectrum for different excitation NIR pump beam diameters $2w_{NIR}$. The transfer function of the system is limited by the aperture defined by the size of the re-focusing parabolic mirror PM_3 (1-inch). In terms of propagation, the plot suggests that the ideal excitation spot size is ∼3 mm.

The transfer function is frequency-dependent and is the result from the division of the on-axis THz field amplitude calculated on the point of interest (the focal point of the last PM_3, where the EO crystal or STM tip is located) divided by the initial field strength (see Eq. 4.1). Thus, the value of H_{prop} indicates how strongly the THz field is enhanced for each THz frequency after the propagation through the optical setup at the final re-focusing point onto the EO crystal or STM tip. In all cases, the results demonstrate that the high THz frequencies propagate more effectively than the low THz frequencies, resulting in stronger field enhancement. That is expected since the low THz frequencies exhibit higher divergence, leading to a less efficient collection, propagation, and re-focusing. The previous plots show that the effect becomes more prominent for smaller excitation beam diameters. Overall, by decreasing the NIR spot size, the propagation and the tight re-focusing become less efficient for every THz frequency component, which is reflected by the total reduction of the transfer function values.

Furthermore, one should note that the aperture of the last parabolic mirror PM_3 limits the transfer function. All calculated curves overlap for excitation beam sizes larger than ∼3 mm. The aperture effect is frequency-

independent and purely geometrical, dictated by the size of the re-focusing parabolic mirror PM_3 (1-inch diameter). This result is also demonstrated in Fig. 4.6, which shows the H_{prop} plotted versus the NIR pump beam diameter $2w_{NIR}$, for selected THz frequencies.

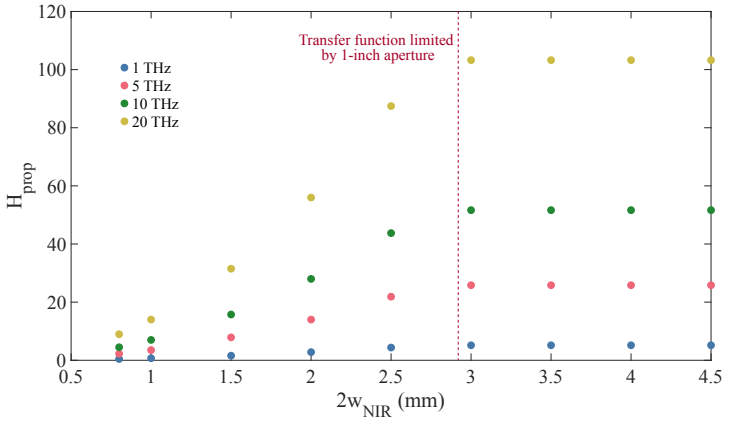

Figure 4.6: Transfer function of propagation H_{prop} versus NIR pump beam diameter $2w_{NIR}$, for selected THz frequencies. The transfer function is limited by the aperture of the re-focusing parabolic mirror PM_3. The aperture effect is purely geometrical: for NIR beam diameters larger than ∼3 mm, the transfer function remains constant for each THz frequency.

The bigger the NIR spot size, the bigger the expanded THz beam reaches the last parabolic mirror PM_3 (see Fig. 4.2, 4.3 and 4.4). Therefore, once the aperture effect is present, by increasing the NIR pump beam diameter (e.g., from 3 mm to 4 mm), a larger part of the THz beam is lost and can not be collected and re-focused by the parabolic mirror PM_3. Nevertheless, from the results demonstrated in the last two plots (see Fig. 4.5 and 4.6), this does not impact the transfer function and thus does not impact the on-axis THz field: for NIR beam diameters larger than ∼3 mm, the calculated value of the transfer function is constant for each THz frequency, independent of the excitation spot size. That result agrees with what is expected as the aperture effect causes the removal of THz power and does not reduce the on-axis field.

To conclude, given just the THz propagation, the ideal NIR pump beam diameter which will provide the highest THz field amplitudes is ∼3 mm. However, this is not the only parameter that needs to be considered. The THz field is expected to scale with fluence, i.e., decrease quadratically with

the NIR pump beam radius. The propagation and the fluence argument are two effects that counter each other.

4.3 Experimental details and data analysis

In the experiment, the STE is excited by the NIR collimated linearly-polarized pulsed laser pump beam under normal incidence from the substrate side. A magnet is mounted above the STE, parallel to the optical table, to saturate the in-plane magnetization. By varying the optical elements of Telescope B (see Table 4.1), different NIR pump spot sizes are tested, and the dependence of the THz field on the excitation spot size is investigated. Since the employed laser source (see Section 2.1) provides a variable repetition rate operation, measurements at 0.5 MHz and 1MHz are conducted, and the emitted THz field in relation to the repetition rate is examined. Table 4.2 gives an overview for the employed configurations of Telescope B; the achieved NIR pump beam diameters ($1/e^2$) and the repetition rates used for each case. For every telescope arrangement, the resulting NIR beam size is characterized in the horizontal direction of the beam with the Knife-edge method (App. A). The measurements are performed closest possible to the STE position.

Telescope B	$2w_{NIR}$ ($1/e^2$)	Repetition rate
Ag plane mirrors	(3.63 ± 0.02) mm	1 MHz
Ag concave mirrors of (100+200 mm) EFL	(1.48 ± 0.03) mm	0.5 MHz
Ag concave mirrors of (50+250 mm) EFL	(1.05 ± 0.03) mm	0.5 MHz, 1MHz
Ag concave mirrors of (50+250 mm) EFL	(0.81 ± 0.03) mm	0.5 MHz, 1MHz

Table 4.2: Employed parameters.

Note that the smallest employed spot size (0.81 ± 0.03) mm is realized by the same telescope configuration used for the third case (Telescope B: Ag concave mirrors of (50+250 mm) EFL). That is possible by moving slightly the linear stage on which the second concave mirror (50 mm EFL)

of Telescope B is mounted, and thus reducing the distance between the two mirrors. Moving the concave mirror out of its optimal position can lead to a non-collimated beam. Nevertheless, the mirror is moved by ∼3 mm. Thus, the divergence of the resulting beam is small enough, and a plane-wavefront excitation can be assumed.

After changing the telescope arrangements, for the variation of the NIR pump spot sizes, each time, a really precise alignment with a camera for the focus and spatial overlap of the probe and THz beam incident onto the electro-optic detection crystal (ZnTe) is performed. For that purpose, the ZnTe is mounted on the linear stage with a magnetic mount. The crystal is replaced temporarily by the camera until the end of the alignment. The magnetic mount allows a reproducible positioning of the crystal, ensuring that the detector is always illuminated in the same spot, and a safe comparison of the experimental data can be made. Then, the crystal has to be placed in the focus position. By moving the linear stage along the propagation axis of the beam, green light generation on the crystal surface indicates the focus position. With that as a reference position, the detector is moved along the propagation axis of the beam in a range within the Rayleigh length of the probe beam, and THz transients are recorded in some positions. Last, the detector is fixed where the optimum signal is observed. However, no significant difference in the measured signals and corresponding spectral amplitudes is observed when moving from the focus position within the Rayleigh length of the probe beam.

For each NIR pump spot size, THz waveforms are measured with EOS detection (see Section 2.3) after excitation with high, intermediate, and low laser pump powers. As expected, the different power values influence mainly the amplitude of the signal and not the waveform shape. The measured THz waveforms with their corresponding spectral amplitudes, obtained via Fourier transform (see Eq. B.1), are displayed in the App. C.1. After ensuring that the waveform peaks do not shift with power, operating at the specific delay where the peaks appear, power scans are performed, and the peak THz signals are recorded. The pump power is controlled by two neutral density filters (ND) linearly varying in optical density. The filters are integrated into the pump beam path on a motorized stage. Also, a chopper wheel chops the THz generation beam (pump beam) for increasing the signal-to-noise ratio with lock-in detection (modulation frequency 607 Hz).

Furthermore, a reference THz waveform is recorded for each data set of the power scan. This trace is used for the 'translation' of the electro-optic

signals S(t) (mV) -which consist raw data- to THz electric fields (kV/cm).

From the electro-optic signals to the THz electric fields incident onto the detector. There is a linear relationship between the measured THz electro-optic signal S(t) and the THz electric field $E_{det}(t)$ incident onto the detector. Particularly, $S(t)$ is the convolution (see Eq. B.3) of the $E_{det}(t)$ with the response function $h_{det}(t)$ of the detection crystal.

$$S(t) = h_{det}(t) * E_{det}(t). \tag{4.2}$$

The response function is determined by the parameters of the employed electro-optic crystal and the sampling pulse [KNW07]. The script used for those calculations is provided by the research group of Tobias Kampfrath. In the code, with the equidistant sampling of the measured $S(t)$ and the calculated $h_{det}(t)$, Eq. 4.2 can be rewritten as an overdetermined matrix equation and numerically solved for $E_{det}(t)$ [SJM+16]. Furthermore, Fourier-transforming (see Eq. B.1) the deconvoluted trace $E_{det}(t)$ yields to the spectral amplitude $E_{det}(\omega)$.

From the numerical simulations of the THz propagation through the optical system, described in Section 4.2, the transfer function of the propagation can be calculated for the given NIR pump beam size. That can be utilized for evaluating the THz fields directly emitted by the spintronic emitter. In this regard, the spectral amplitude $E_{STE}(\omega)$ emitted directly by the STE is considered as the input to the optical system, and the spectral amplitude $E_{det}(\omega)$ incident onto the detector as the output.

From the THz electric fields incident onto the detector to the THz electric fields directly emitted by the STE. To proceed from the deconvoluted THz field spectrum $E_{det}(\omega)$ incident on the detector to the THz electric field spectrum $E_{STE}(\omega)$ directly emitted by the STE, we note that those two quantities are connected by the transfer function $H_{prop}(\omega)$,which captures the propagation through the optical setup, as follows

$$E_{det}(\omega) = E_{STE}(\omega)H_{prop}(\omega). \tag{4.3}$$

This approach assumes a perfect alignment of the whole optical setup and perfect Gaussian beams. The $H_{prop}(\omega)$ is calculated as described in Section 4.2 for all employed NIR pump spot sizes. Figure 4.7 depicts the results.

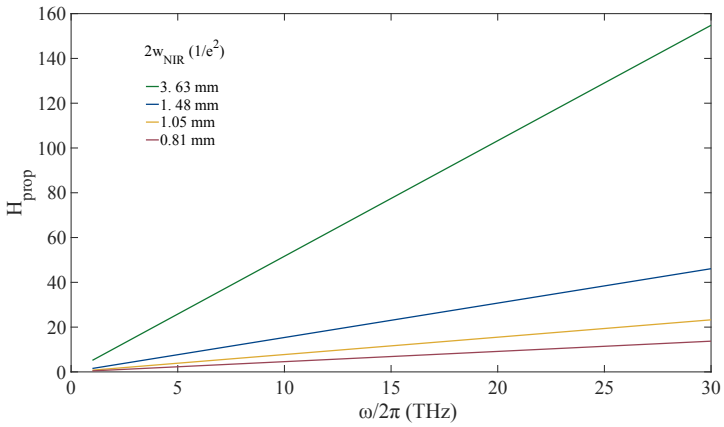

Figure 4.7: The transfer function of propagation H_{prop} is numerically calculated and plotted versus the THz frequency spectrum for the four employed experimentally defined excitation NIR pump beam diameters $2w_{NIR}$.

Also, the beam radius of the THz frequencies along the propagation axis is numerically calculated and plotted for all used pump spot sizes. The results can be found in App. C.2. For simplicity, only selected frequency components are depicted.

All the measured and the deconvoluted reference THz waveforms, with their corresponding spectral amplitudes, are shown in App. C.1.2. Relating the peaks of the measured and resulting deconvoluted waveforms, two conversion factors are extracted and rescale the power scan data from S to E_{det} (factor a) and from E_{det} to E_{STE} (factor b). All the above-described processes is summarized in the flowchart of Fig. 4.8. In this diagram, the THz traces of (1.48 ± 0.03) mm NIR pump spot size are used as an example.

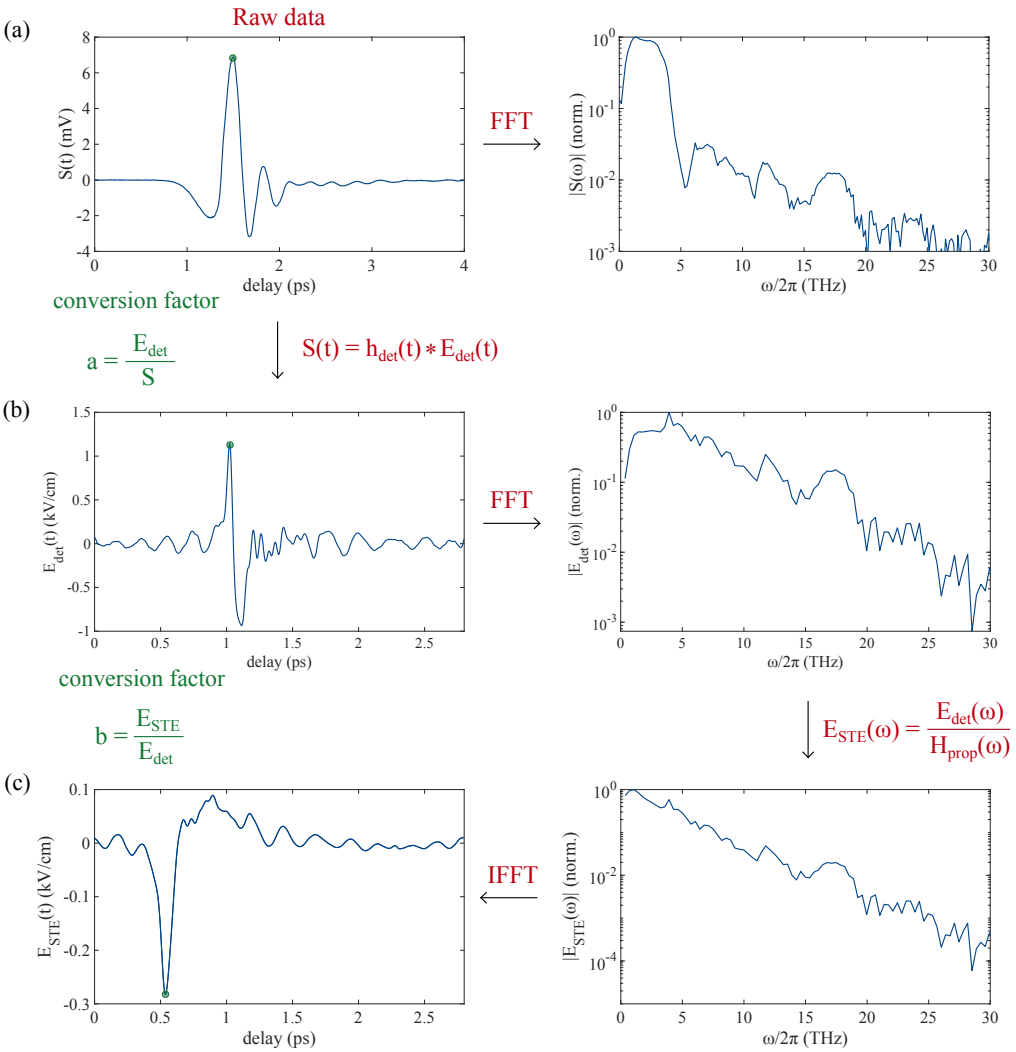

Figure 4.8: Flowchart of the data analysis. (a) Measured and (b), (c) deconvoluted reference THz waveforms, with their corresponding spectral amplitudes. The measured electro-optic signal S(t) is obtained after excitation with (1.48 ± 0.03) mm NIR pump spot size, 740 W average power, and operating at 0.5 MHz repetition rate.

4.4 Results and discussion

As it is summarized in Table 4.2, three NIR pump spot sizes are employed for the excitation of the spintronic emitter operating at 0.5 MHz and three at 1 MHz repetition rate. Based on the data analysis described in Section 4.3 the THz electric field amplitudes E_{det} incident onto the detection crystal, and then the emitted THz fields E_{STE} are extracted from the measured electro-optic signals S(t). A characteristic example of the deconvoluted THz waveform traces is depicted in Fig. 4.9.

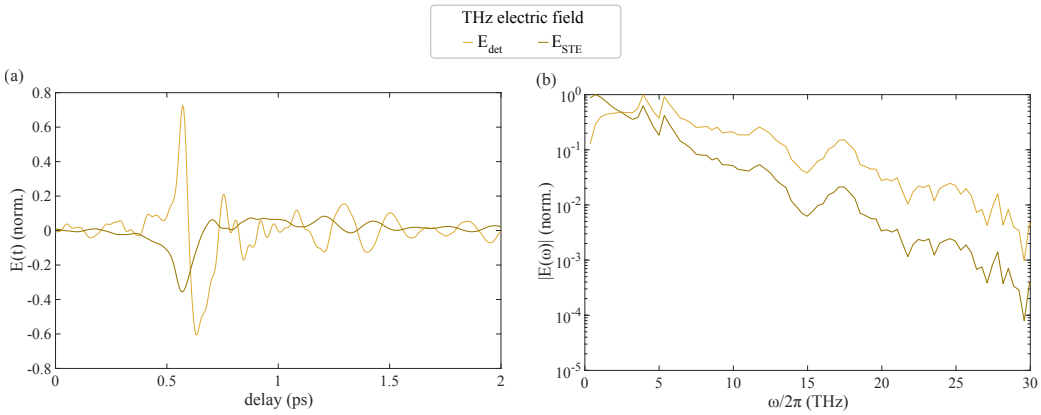

Figure 4.9: (a)Deoconvoluted THz waveforms with their (b) corresponding spectral amplitudes of the THz field incident onto the detector E_{det} and the emitted THz field E_{STE}. The measured electro-optic signal, from where the depicted traces are extracted as described in Section 4.3, is obtained after excitation with 1.05 mm NIR pump spot size, 0.5 MHz repetition rate operation and 518 W pump power.

In this section, the results of the powers scans performed for each case are compared and discussed. Relating the peaks of the measured and resulting deconvoluted waveforms, two conversion factors are extracted and rescale the power scan data from S to E_{det} (factor a) and from E_{det} to E_{STE} (factor b) as depicted in Fig. 4.8. The first part of this section deals with the dependence of the THz field on the NIR pump spot size used to excite the STE. In the second part, the THz field scaling under variable repetition rate operation is examined.

4.4.1 Dependence of the THz field on the pump spot size

THz field incident onto the detector

Based on the data analysis described in Section 4.3 the THz electric field amplitudes E_{det} incedent onto the detection crystal are extracted from the measured electro-optic signals S(t). Fig. 4.10 shows the THz electric field E_{det} plotted versus (a) fluence and (b) average power, measured for three NIR pump spot sizes at 0.5 MHz repetition rate. In the curves of Figure 4.10(a) sublinear fits (see Eq. 3.3) are applied.

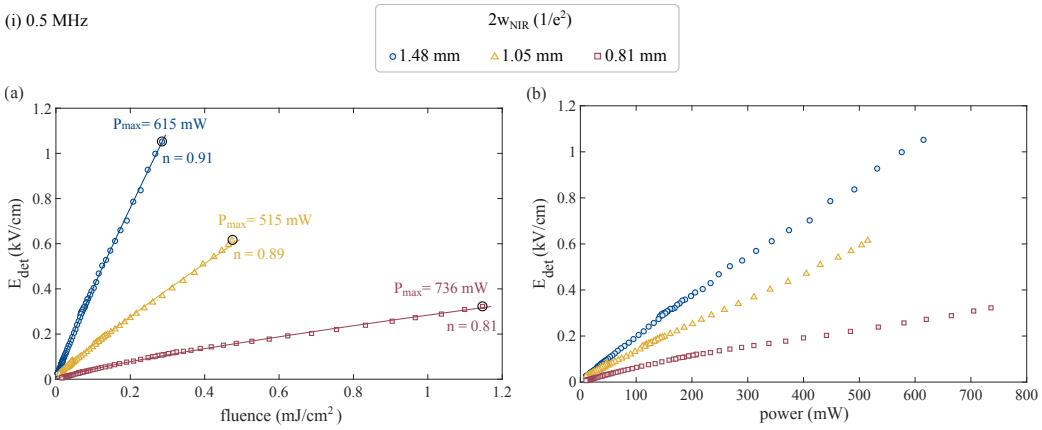

Figure 4.10: THz electric field E_{det} incident onto the electro-optic detection crystal versus (a) fluence and (b) average power measured for three different NIR pump spot sizes at 0.5 MHz repetition rate. In plot (a), the lines are sublinear fits to the experimental data, and the fitted parameters n are depicted. Also, for each case, the maximum employed average power is indicated.

First, nearly linear fluence/power scaling is observed for all excitation spot sizes. There is no significant saturation for any case, which is also indicated from the fitted n parameters whose values are close to one. The curve for the smallest employed spot size (0.81 mm) deviates a bit more from the linear scaling, and a slight change of the slope occurs around 0.3 mJ/cm^2 fluence value. Second, considering vertical cuts through the plots of Fig. 4.10, the next observation is that the THz electric field at the detector increases with increasing NIR pump spot size at constant fluence/power. That is

attributed to propagation effects and tighter re-focusing on the detector, which occurs for larger excitation pump beams (see Section 4.2).

Fig. 4.11 shows the THz electric field E_{det} plotted versus (a) fluence and (b) average power, measured for three NIR pump spot sizes at 1 MHz repetition rate. In the curves of Fig. 4.11(a) sublinear fits (see Eq. 3.3) are applied.

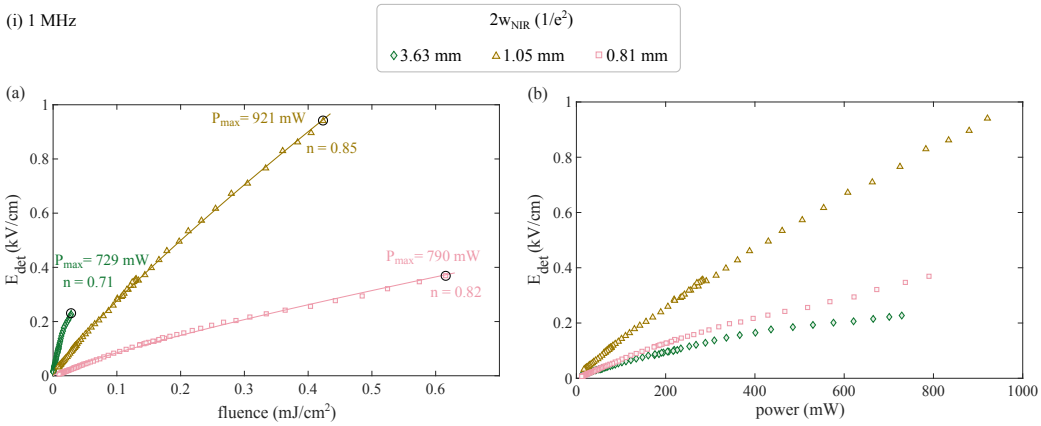

Figure 4.11: THz electric field E_{det} incident onto the electro-optic detection crystal versus (a) fluence and (b) average power measured for three different NIR pump spot sizes at 1 MHz repetition rate. In plot (a), the lines are sublinear fits to the experimental data, and the fitted parameters n are depicted. Also, for each case, the maximum employed average power is indicated.

First, nearly linear scaling is observed for the curves of the small (0.81 mm) and intermediate (1.05 mm) employed NIR pump beams, similar to the previous results for 0.5 MHz repetition rate (see Fig. 4.10). However, the curve for the biggest spot size (3.63 mm) exhibits a sublinear scaling (n=0.71). That might be assigned to the plasma generation from the tightly focused residual NIR pump beam in the THz beam expansion telescope (PM_1 and PM_2). Because of limited space, the Si wafer, which filters out the remaining NIR pump beam, is placed after the parabolic mirror PM_2 (see Fig. 4.1). Therefore, the optical pump beam is tightly focused within the telescope -together with the THz beam- generating plasma. Compared to the other used pump beam spots, in this case, the plasma generation is more prominent since the larger the NIR beam reaching the PM_1, the tighter the resulting focus. The plasma is a local effect and happens in a small area defined by the NIR beam waist in the focus position. Thus, a tiny fraction of the focused THz beam experiences it. Since the high THz

frequencies are the ones focused tighter (see Fig. C.11), it is expected that they are going to be the ones affected stronger. The plasma could be seen during the experiments, but we cannot quantify its effect.

Furthermore, in Fig. 4.11(a), the THz electric field at the detector increases with increasing NIR pump spot size at constant fluence, similarly to the previous results for 0.5 MHz repetition rate (see Fig. 4.10(a)). Note that the green curve, which corresponds to the largest employed pump spot (3.63 mm), is limited to small fluence values because of the limited available laser power. With a laser source delivering larger average powers, larger fluence values could be achieved, thus even larger THz fields. On the other hand, in Fig. 4.11(b) where the E_{det} is plotted versus the average power, the field amplitude for the largest employed pump beam exhibits lower values when compared with the other two cases. That reflects that the emitted THz field scales with fluence, i.e., decreases quadratically with the pump beam radius.

Balancing between the excitation fluence and THz propagation is required for achieving the highest THz fields on the detector. To summarize is helpful to look at the Eq. 4.3. The THz field at the detector is determined by the emitted THz field from the STE and the THz propagation through the optical system. The propagation predicts that up to a certain pump spot size value, limited by the aperture of the re-focusing parabolic mirror PM_3, the THz electric field incident onto the detector increases with increasing pump spot size (see Section. 4.2). On the other hand, opposite to this, the emitted THz field from the STE is expected to scale with fluence, and thus to scale down quadratically with the pump spot size (see Eq. 3.2). From Fig. 4.10(a) and Fig. 4.11(a) it seems that the THz propagation dominates the THz field on the detector. In our specific setup geometry, the option of increasing the fluence by decreasing the pump spot size does not provide the best performance in terms of the measured THz fields since small pump spot sizes prohibit tight focusing on the detector due to smaller beam expansion (by the expansion telescope realized by PM_1 and PM_2). On the contrary, too large pump beams can yield reduced fields as a result of limited fluence/power. Due to those two competing effects, an optimum NIR pump spot size should exist for the specific setup. The biggest employed pump beam (3.63 mm) lies above the optimum value, and the rest used pump spot sizes below. Testing more excitation beam sizes is not possible because of the limited telescope arrangements in the setup.

THz field emitted by the spintronic emitter

Proceeding with the data analysis as described in the previous section, the propagation effects are eliminated by utilizing the simulated transfer function (see Eq. 4.3), and the THz field emitted by the STE is calculated. Thus, a further understanding of its fluence/power scaling under excitation with different pump beam sizes is examined. Figure 4.12 shows the emitted THz electric field E_{STE} plotted versus (a) fluence and (b) average power for the three employed NIR pump spot sizes at 0.5 MHz repetition rate.

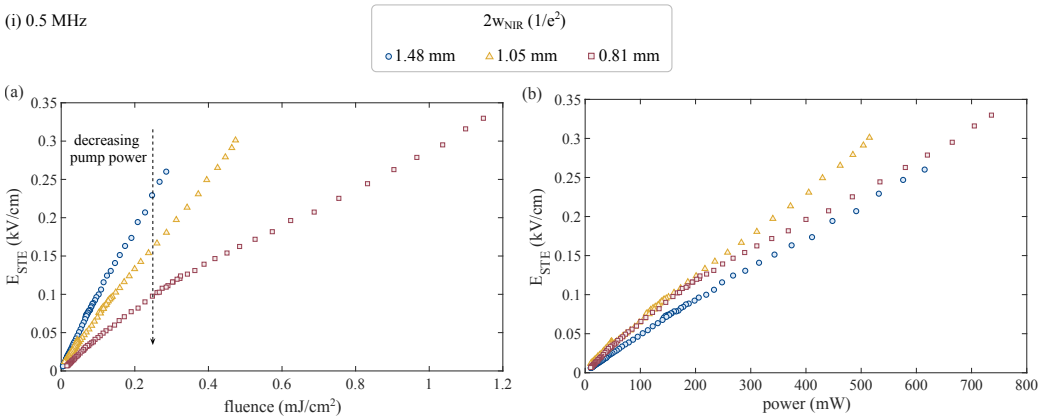

Figure 4.12: Emitted THz electric E_{STE} from the spitronic emitter versus (a) fluence and (b) average power, for three different pump spot sizes at 0.5 MHz repetition rate.

When comparing different pump spot sizes, the results suggest that the emitted THz field is constant at constant power and not fluence. That is opposite to the expectations. Particularly, in Fig. 4.12(a), the field exhibits the largest values under constant fluence with increasing pump spot size. The emitted THz field is expected to scale with the fluence, and thus to scale down quadratically with the pump spot size at a fixed power. In this regard, it is helpful to remember the previously provided Eq. 3.2. In Fig. 4.12(b), a slight reduction of the field under constant power is observed for 1.48 mm pump beam size. However, it is not reduced as much as expected for a reduced fluence in comparison to the fields achieved with the other pump beams.

Figure 4.12 shows the emitted THz electric field E_{STE} plotted versus (a) fluence and (b) average power for the three employed NIR pump spot sizes at 1 MHz repetition rate.

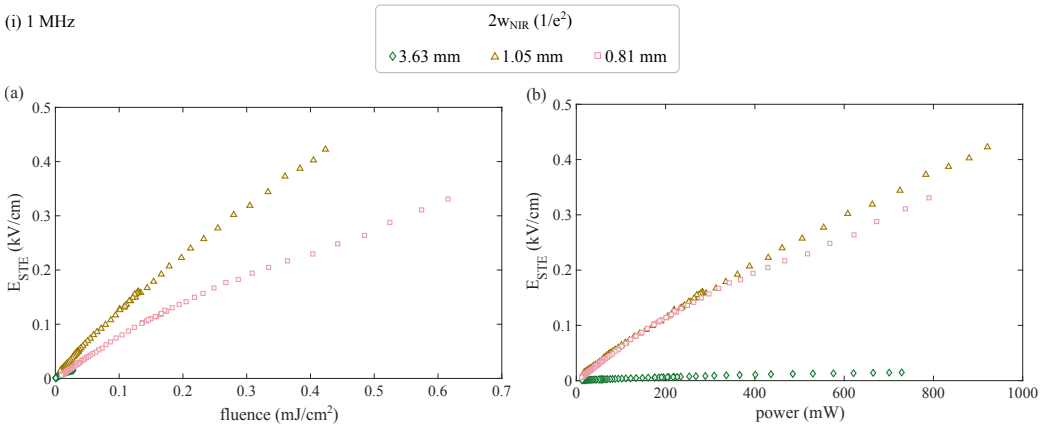

Figure 4.13: Emitted THz electric E_{STE} from the spitronic emitter versus (a) fluence and (b) average power, for three different pump spot sizes at 1 MHz repetion rate.

Similar to the previous results, for 1.05 mm and 0.81 mm pump spot size, the emitted THz field is constant under constant power and not fluence. However, it is significantly decreased for the 3.63 mm pump beam when plotted versus power. In this case, the field is reduced as expected for a reduced fluence compared with the other cases.

Overall, we find that for the smaller employed pump beams, the emitted THz field is determined by the power and not the fluence, i.e., it is independent of spot size. However, at the larger used pump beam (see 3.63 mm @1 MHz on Fig. 4.13(b)), the field is reduced as expected for a reduced fluence.

A possible explanation for this deviation could occur from the propagation properties of the THz radiation. For pump beams much smaller than the THz wavelengths, the wave propagation is diffraction limited. The research of Dreyhaupt *et al.* [DWHD06] on the THz radiation produced by photoconductive switches demonstrates that the THz emission exhibits different dependencies on the pump spot size in the following two limiting cases

$$\text{(A)} \quad \boldsymbol{w_{NIR} \gg \lambda_{THz}}: \quad P_{THz} \propto \frac{P_{NIR}^2}{w_{NIR}^2} \quad \Rightarrow \quad E_{THz} \propto \frac{P_{NIR}}{\pi w_{NIR}^2} \tag{4.4}$$

$$\text{(B)} \quad \boldsymbol{w_{NIR} \ll \lambda_{THz}}: \quad P_{THz} \propto P_{NIR}^2 w_{NIR}^2 \quad \Rightarrow \quad E_{THz} \propto P_{NIR}. \quad (4.5)$$

Eq. 4.4 and Eq. 4.5 are derived from the results and formulas shown in that work. P_{NIR} is the excitation average power, and w_{NIR} is the pump beam radius. P_{THz} and E_{THz} are the emitted THz power and field, respectively. For the transition from the P_{THz} to E_{THz} the proportionality $P_{THz} \propto E_{THz}^2 \pi w_{NIR}^2$ is considered. The regime (A), where the employed pump spot size is much bigger than the THz wavelengths, is expected by the normal emission: the emitted THz field scales with fluence thus scales down quadratically with the pump beam radius at fixed power. On the other hand, on the regime (B), for an excitation spot size much smaller than the THz wavelengths, the emitted THz field is determined by the power, and it is spot size independent. Even though our results could suggest such an explanation, since for the small used pump beams (0.81 mm, 1.05 mm, 1.48 mm), the field scales with power, and for the largest pump beam (3.63 mm) scales with fluence, there is no indication that we operate into the sub-diffraction regime. All employed pump spot sizes are larger than the wavelengths of the emitted THz spectrum, which approximately ranges from 300 μm to 10 μm. There is uncertainty on the measured pump beam sizes, as they are characterized just on the horizontal axis of the beam, and maybe they are not measured exactly to the STE's position. However, the errors are not so large that the measured values could be in the sub-diffraction limit. Moreover, a transition from the diffraction-limited regime to the normal emission regime should cause measurable changes in the spectral amplitudes. The low frequencies -having bigger wavelengths- are more sensitive to the subwavelength volumes when the pump spot size gets smaller; thus, the short wavelengths propagate more efficiently to the far-field. Therefore, a blue-shifted spectrum should be observed moving to smaller excitation spots. Based on the deconvoluted spectral amplitudes on Fig. C.7 and Fig. C.10 this is not observed.

Experimental difficulties and errors can also cause deviations from the expected scaling. The alignment of the beams on the detection crystal has a crucial role in the measurements. The THz electric field is a local quantity that varies over the pump spot. If perfect aligmnent and a 'point'-probe beam are assumed (see Section 2.3, Fig. 2.6), the observable of the electro-optic sampling detection is the (on-axis) THz field at the spot center. However, in case of an 'non-point'-probe, i.e., a large focused probe beam a THz field average over the probe spot is measured instead of the

on-axis field, which could cause deviations from the expected scaling. Nevertheless, a careful and precise alignment of the probe and THz beam on the electro-optic detection crystal is done (see Section 4.3), and confidently a 'point'-like probe can be assumed in the performed experiments. Therefore, it is unlikely to explain the observed deviations from that point of view.

Last, the emitted THz field is obtained through the use of the numerically calculated transfer function of propagation (see Section 4.3, Eq. 4.3). This approach assumes a perfect alignment of the whole optical setup and perfect Gaussian beams. In reality, though, those assumptions may are not absolutely accurate. The validity of the transfer function is not yet tested. However, that is a crucial component that will allow safe conclusions about the scaling of the emitted THz field with power/fluence. In Fig. 4.14 one of the extracted THz waveforms of the emitted THz field E_{STE} is plotted. Together with it, a THz transient of the emitted THz field obtained in an 80 MHz oscillator system, provided by the research group of Tobias Kampfrath, is depicted and used as a reference for comparisons. Similar traces can be found on [RBN+21], [JCGN+21]. The curves are normalized to their minima.

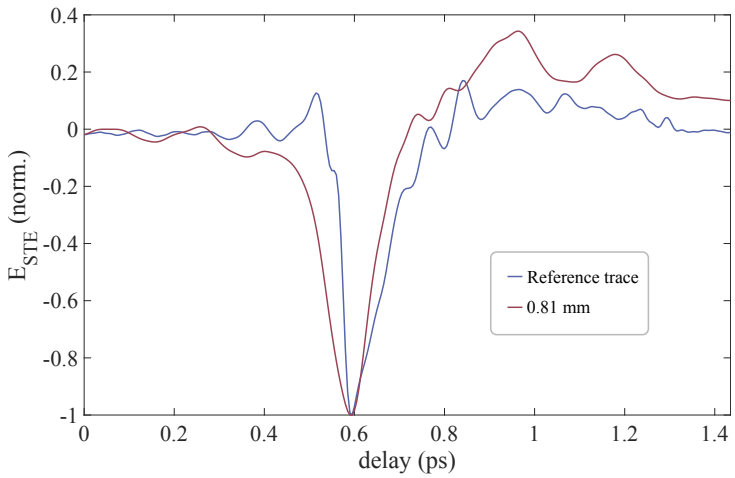

Figure 4.14: THz transients of the emitted field E_{STE}. The red curve is extracted from the signal measured at 0.81 mm NIR pump spot size at 0.5 MHz repetition rate operation. The blue curve is used as a reference for shape comparison. The curves are normalized to their minima.

We obtain a very similar THz waveform shape as the reference curve. That is an indication that the frequency-dependence of the transfer function is correct. However, further work is needed to test the validity of the transfer

function and clarify its role for the observed scalings. For that purpose, the use of well-understood THz emitters, like ZnTe or GaP, where one precisely knows what to expect, can help. Such measurements are not performed in this thesis.

4.4.2 Dependence of the THz field on the repetition rate

Based on the data analysis described in Section 4.3 the THz electric field amplitudes E_{det} incident onto the detection crystal are extracted from the measured electro-optic signals S(t). Fig. 4.15 shows the THz electric field E_{det} plotted versus (a) the pulse energy and (b) the average power, measured for 0.81 mm NIR pump spot size at variable repetition rates of 0.5 MHz and 1 MHz.

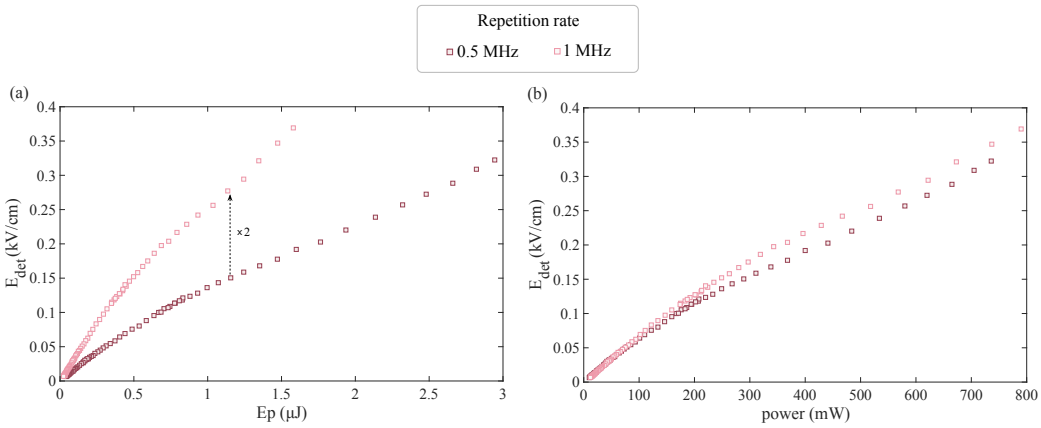

Figure 4.15: THz electric field E_{det} incident onto the electro-optic detection crystal versus (a) pulse energy and (b) average power measured for 0.81 mm NIR pump spot sizes at variable repetition rates of 0.5 MHz and 1 MHz.

First, no saturation effects and identical power scaling for both repetition rates are observed. This demonstrates that no single-pules saturation effects are present. Second, the results suggest that for a constant pump spot size and variable repetition rate, the THz electric field at the detector is constant for constant power and not pulse energy. That is contrary to the expectations. Specifically, in Fig. 4.15 when the field is plotted versus pulse energy, it exhibits almost double field amplitudes for 1 MHz repetition rate operation. Measurements with varying the repetition rate are performed for

1.05 mm pump spot size as well (see Table 4.2). However, since they exhibit similar behavior are not presented here.

The THz field, in contrast to THz power, depends only on properties of the single pulse as pulse energy, pulse duration, and fluence, but not on an average quantity such as the pump power. The strength of the emitted THz field is proportional to the induced current in the STE, which relates to the number of carriers excited per pulse. The number of excited electrons is a function of the energy absorbed in the metallic layer during the pulse. If the repetition rate at constant power is doubled, as in this case, from 0.5 MHz to 1 MHz, a single pulse has only half of the energy content. Therefore, the induced current and thus the emitted THz field should be reduced by a factor of two. That is accurate only if the pulses can be considered isolated, i.e., there are no memory effects between two successive pulses. In this case, with MHz repetition rates operation, the time between two pulses is in the range of 1μs. In this time frame, the STE should have completely relaxed to its ground state before the next pulse arrives; thus, there are no memory effects expected. Hence for a constant pump spot size and variable repetition rate, the THz field is expected to stay constant for constant pulse energy and not power. The opposite observation can be explained just by assuming that there is a factor of two missing in the calibration/analysis process, which is not easy to identify up to now.

Chapter 5

Conclusions and Outlook

The work presented here attempts to define optimized excitation conditions for the spintronic THz emitter (STE), aiming at high THz electric field amplitudes for THz-STM application, at MHz repetition rates, and microjoules pulse energies.

The THz-gated scanning tunneling microscopy enables the study of ultrafast dynamics of optical excited systems with femtosecond temporal and atomic-level spatial resolution. In this technique, the electric field of a single-cycle THz pulse acts as a quasi-static bias voltage modulation of the STM junction, resulting in a time-dependent current response. An essential ingredient for obtaining measurable currents in the THz-STM is the high repetition rate of the laser source. In this respect, repetition rates in the MHz range are desirable. Moreover, to get sufficient THz bias, THz-STM demands high incident THz fields at the STM tip ($\sim$ kV/cm). With a parabolic mirror integrated into the STM platform, the THz pulses are focused at the STM tip, enhancing the THz field amplitudes. Furthermore, the achieved time resolution in THz-STM is defined by the temporal variation of the THz pulse. Besides other advantages, the STE is a very well-suited THz source for THz-STM due to its fast transients and extremely large bandwidth, which enable very fast voltage modulation in the STM, increasing the achievable time resolution.

In this work, an OPCPA (Optical Parametric Chirped-pulse Amplification) laser system is employed. It is an amplified laser system, which delivers ultrashort laser pulses of $\sim$8 fs duration, centered at 800 nanometers. It operates with a variable high repetition rate of 0.5 MHz or 1 MHz, resulting in 6 μJ or 3 μJ pulse energies, respectively. Through the THz excitation setup, we aim to achieve high THz electric field amplitudes at the STM tip. To

meet that goal, optimizing the excitation fluence for the STE -at the given laser parameters-, for achieving high emitted THz powers is required. At the same time, an efficient THz propagation through the optical setup is necessary for tight focusing onto the STM tip, where the strong confinement of the THz radiation will result in enhanced THz field amplitudes.

The initially employed excitation geometry of the STE, in combination with the laser parameters, causes several unwanted effects which limit the THz emission and propagation efficiency, making it hard to achieve high THz fields. In that geometry, the STE can be excited under normal incidence at any position along a tightly focused NIR pump beam, providing the flexibility to vary the pump spot size and fluence incident to the emitter. Placing the STE inside or close to the NIR focus for excitation with small spot sizes and, thus, high fluence, ablation can irreversibly damage the spintronic emitter with increasing power. Moreover, in that regime, saturation effects and emission from subwavelength volumes can drastically reduce the emission efficiency of the STE, leading to smaller THz field amplitudes. For excitation with larger spot sizes that will help handle those effects better, the emitter is placed further away from the NIR focus position. In turn, this gives rise to strong chromatic aberrations, leading to inefficient propagation of the THz radiation inside the optical setup and finally inefficient re-focusing onto the STM tip, which drastically reduces the achievable THz amplitudes.

After attempting to disentangle those effects through measurements and simulations, a new optimized excitation geometry is designed and built based on the acquired knowledge. The new geometry enables the use of different NIR pump beam sizes. Thus, optimum THz propagation and excitation conditions, which will provide higher THz fields amplitudes, are investigated. Furthermore, the STE is now excited with a collimated NIR pump beam to reduce chromatic aberrations. The off-axis parabolic mirror required for re-focusing the beam onto the detection crystal is restricted by the STM geometry. Thus it is chosen to be identical to the one integrated into the STM platform. For tight focusing of the THz beam onto the STM tip or the detection crystal, the THz beam size is expanded to match the size of the re-focusing parabolic mirror through an expansion telescope.

In the experiments, three NIR pump spot sizes are employed for the excitation of the spintronic emitter operating at 0.5 MHz and three at 1 MHz repetition rate. The THz radiation is detected through the electro-optic sampling technique. For each case, power scans are performed. After data analysis, the THz electric field amplitudes E_{det} incident onto the detec-

tion crystal are extracted from the measured electro-optic signals S(t). The THz field incident onto the detector or the STM tip depends on the emitted THz field from the STE and the THz propagation through the optical system. Therefore, achieving the highest THz field at the experiment requires balancing the excitation fluence and the efficiency of the THz propagation. The results demonstrate that the THz propagation dominates the THz field on the detector. In our specific setup geometry, increasing the fluence by decreasing the pump spot size does not necessarily provide the best performance in terms of the measured THz fields since the small pump spot sizes prohibit tight focusing on the detector due to smaller beam expansion. On the contrary, too large pump beams can yield a reduced field due to limited available fluence/power. Due to those two competing effects, an optimum NIR pump spot size should exist for the specific setup. The results show that the biggest employed pump spot size lies above the optimum value, and the other used pump beam sizes below. Because of limited telescope arrangments, which enables the variation of the pump spot size, testing more beam values was not possible in the experiments.

Furthermore, after numerical simulations modeling the THz propagation through the optical system, the transfer function of propagation is calculated. Therefore, by employing the numerically calculated transfer function, the propagation effects are eliminated, and the emitted THz field is extracted. The results demonstrate that the THz field emitted by the STE scales with the average power for the smaller employed pump beams, independent of the spot size. On the contrary, for the largest employed pump spot size, the emitted THz field scales with the fluence, as expected. That difference can be assigned to a diffraction-limited emission for cases where the pump spot size is much smaller than the THz wavelengths. More measurements with more pump spot sizes are required to confirm that assumption and ensure that the observed behavior is not an artifact. Unfortunately, the limited telescope arrangement with which the NIR pump spot size is varied does not allow testing more pump beams in the current setup. Therefore, that could be a task of future work. Furthermore, an essential factor that will allow us to draw safe conclusions about the emitted THz filed scaling is validating the modeled transfer function employed to extract the fields. For that purpose, the use of well-understood THz emitters, like ZnTe or GaP, where one precisely knows what to expect, can help. However, such measurements are not within the scope of this thesis, and they could be a task of future work.

Finally, the THz field dependence on the repetition rate is examined.

First, no saturation effects and identical power scaling for varying repetition rates are observed. This indicates that no single-pules saturation effects are present in our conditions. Moreover, the results show that for a constant pump spot size and variable repetition rate, the THz electric field at the detector is constant for constant power and not pulse energy. That is opposite to the expectations. We assume that there is a factor of two missing in the analysis, which could not be identified.

Currently, a new laboratory is being built in the group, where a different laser system is installed, and the excitation conditions of the STE have to be defined. Based on a solid-state laser (CARBIDE laser from Light Conversion), it provides pulses of $\sim$ 200 fs duration, centered at 1030 nm. The pulses are spectrally broadened by a multiplate compressor and subsequently recompressed, eventually resulting in $\sim$ 35 fs duration. It can operate at a variable repetition rate of 1 MHz and 2 MHz, delivering 40 μJ and 20 μJ pulse energies, respectively. As demonstrated, to avoid saturation effects on the STE, a critical fluence should not be exceeded. The limiting fluence threshold, which is the critical fluence before saturation effects occur, is $\sim$1 mJ/cm^2 [VOM+21]. An ideal pump spot size also depends on the available pump power. Since the new laser system provides larger average powers than the one employed in this work, based on the results presented here, we can operate the STE at a large pump beam size which is efficient for optimized THz propagation. Therefore, the new laser system allows us to operate at optimized fluence and THz propagation without subwavelength effects and minimized aberrations.

Bibliography

[ald15] "Laser and gaussian beam propagation and transformation." CRC Press, Sep. 2015, pp. 1–15. [Online]. Available: https://doi.org/10.1081/e-eoe2-120009751

[Boy20] R. W. Boyd, *Nonlinear Optics*. Elsevier, 2020. [Online]. Available: https://doi.org/10.1016/c2015-0-05510-1

[DWHD06] A. Dreyhaupt, S. Winnerl, M. Helm, and T. Dekorsy, "Optimum excitation conditions for the generation of high-electric-field terahertz radiation from an oscillator-driven photoconductive device," *Optics Letters*, vol. 31, no. 10, p. 1546, May 2006. [Online]. Available: https://doi.org/10.1364/ol.31.001546

[FQW+21] Z. Feng, H. Qiu, D. Wang, C. Zhang, S. Sun, B. Jin, and W. Tan, "Spintronic terahertz emitter," vol. 129, no. 1, p. 010901, Jan. 2021. [Online]. Available: https://doi.org/10.1063/5.0037937

[FTKL04] J. Faure, J. V. Tilborg, R. A. Kaindl, and W. P. Leemans, "Modelling laser-based table-top THz sources: Optical rectification, propagation and electro-optic sampling," *Optical and Quantum Electronics*, vol. 36, no. 8, pp. 681–697, Jun. 2004. [Online]. Available: https://doi.org/10.1023/b:oqel.0000039617.85129.c2

[FZ02] B. Ferguson and X.-C. Zhang, "Materials for terahertz science and technology," vol. 1, no. 1, pp. 26–33, Sep. 2002. [Online]. Available: https://doi.org/10.1038/nmat708

[Goo05] J. W. Goodman, *Introduction to Fourier optics*. Roberts and Company Publishers, 2005.

[JCGN+21] P. Jiménez-Cavero, O. Gueckstock, L. Nádvorník, I. Lucas, T. S. Seifert, M. Wolf, R. Rouzegar, P. W. Brouwer,

S. Becker, G. Jakob *et al.*, "Tuning laser-induced terahertz spin currents from torque-to conduction-electron-mediated transport," *arXiv preprint arXiv:2110.05462*, 2021. [Online]. Available: https://arxiv.org/abs/2110.05462

[KBM+13] T. Kampfrath, M. Battiato, P. Maldonado, G. Eilers, J. Nötzold, S. Mährlein, V. Zbarsky, F. Freimuth, Y. Mokrousov, S. Blügel, M. Wolf, I. Radu, P. M. Oppeneer, and M. Münzenberg, "Terahertz spin current pulses controlled by magnetic heterostructures," vol. 8, no. 4, pp. 256–260, Mar. 2013. [Online]. Available: https://doi.org/10.1038/nnano.2013.43

[KNW07] T. Kampfrath, J. Nötzold, and M. Wolf, "Sampling of broadband terahertz pulses with thick electro-optic crystals," *Applied Physics Letters*, vol. 90, no. 23, p. 231113, Jun. 2007. [Online]. Available: https://doi.org/10.1063/1.2746939

[Kog65] H. Kogelnik, "On the propagation of gaussian beams of light through lenslike media including those with a loss or gain variation," vol. 4, no. 12, p. 1562, Dec. 1965. [Online]. Available: https://doi.org/10.1364/ao.4.001562

[Mal17] J. Malter, "Characterization of a nanotip electron source for femtosecond point-projection microscopy," 2017.

[Mit17] D. M. Mittleman, "Perspective: Terahertz science and technology," vol. 122, no. 23, p. 230901, Dec. 2017. [Online]. Available: https://doi.org/10.1063/1.5007683

[MSKW20] M. Müller, N. M. Sabanés, T. Kampfrath, and M. Wolf, "Phase-resolved detection of ultrabroadband THz pulses inside a scanning tunneling microscope junction," *ACS Photonics*, vol. 7, no. 8, pp. 2046–2055, Jul. 2020. [Online]. Available: https://doi.org/10.1021/acsphotonics.0c00386

[NH06] L. Novotny and B. Hecht, *Principles of Nano-Optics*. Cambridge University Press, 2006. [Online]. Available: https://doi.org/10.1017/cbo9780511813535

[NSS+19] D. M. Nenno, L. Scheuer, D. Sokoluk, S. Keller, G. Torosyan, A. Brodyanski, J. Lösch, M. Battiato, M. Rahm, R. H.

Binder, H. C. Schneider, R. Beigang, and E. T. Papaioannou, "Modification of spintronic terahertz emitter performance through defect engineering," vol. 9, no. 1, Sep. 2019. [Online]. Available: https://doi.org/10.1038/s41598-019-49963-8

[PB20] E. T. Papaioannou and R. Beigang, "THz spintronic emitters: a review on achievements and future challenges," vol. 10, no. 4, pp. 1243–1257, Dec. 2020. [Online]. Available: https://doi.org/10.1515/nanoph-2020-0563

[RBN+21] R. Rouzegar, L. Brandt, L. Nadvornik, D. Reiss, A. Chekhov, O. Gueckstock, C. In, M. Wolf, T. Seifert, P. Brouwer *et al.*, "Laser-induced terahertz spin transport in magnetic nanostructures arises from the same force as ultrafast demagnetization," *arXiv preprint arXiv:2103.11710*, 2021. [Online]. Available: https://arxiv.org/abs/2103.11710

[Sie86] A. E. Siegman, *Lasers*. University Science Books, 1986.

[SJM+16] T. Seifert, S. Jaiswal, U. Martens, J. Hannegan, L. Braun, P. Maldonado, F. Freimuth, A. Kronenberg, J. Henrizi, I. Radu, E. Beaurepaire, Y. Mokrousov, P. M. Oppeneer, M. Jourdan, G. Jakob, D. Turchinovich, L. M. Hayden, M. Wolf, M. Münzenberg, M. Kläui, and T. Kampfrath, "Efficient metallic spintronic emitters of ultrabroadband terahertz radiation," vol. 10, no. 7, pp. 483–488, May 2016. [Online]. Available: https://doi.org/10.1038/nphoton.2016.91

[SJS+17] T. Seifert, S. Jaiswal, M. Sajadi, G. Jakob, S. Winnerl, M. Wolf, M. Kläui, and T. Kampfrath, "Ultrabroadband single-cycle terahertz pulses with peak fields of 300 kV cm-1from a metallic spintronic emitter," vol. 110, no. 25, p. 252402, Jun. 2017. [Online]. Available: https://doi.org/10.1063/1.4986755

[SSGG13] D. M. Slocum, E. J. Slingerland, R. H. Giles, and T. M. Goyette, "Atmospheric absorption of terahertz radiation and water vapor continuum effects," *Journal of Quantitative Spectroscopy and Radiative Transfer*, vol. 127, pp. 49–63, Sep. 2013. [Online]. Available: https://doi.org/10.1016/j.jqsrt.2013.04.022

[ST19] B. E. Saleh and M. C. Teich, *Fundamentals of photonics*. john Wiley & sons, 2019.

[STG+18] T. S. Seifert, N. M. Tran, O. Gueckstock, S. M. Rouzegar, L. Nadvornik, S. Jaiswal, G. Jakob, V. V. Temnov, M. Münzenberg, M. Wolf, M. Kläui, and T. Kampfrath, "Terahertz spectroscopy for all-optical spintronic characterization of the spin-hall-effect metals pt, w and cu80ir20," *Journal of Physics D: Applied Physics*, vol. 51, no. 36, p. 364003, Aug. 2018. [Online]. Available: https://doi.org/10.1088/1361-6463/aad536

[Sve10] O. Svelto, *Principles of Lasers*. Springer US, 2010. [Online]. Available: https://doi.org/10.1007/978-1-4419-1302-9

[THKH21] T. Tachizaki, K. Hayashi, Y. Kanemitsu, and H. Hirori, "On the progress of ultrafast time-resolved THz scanning tunneling microscopy," *APL Materials*, vol. 9, no. 6, p. 060903, Jun. 2021. [Online]. Available: https://doi.org/10.1063/5.0052051

[Ton07] M. Tonouchi, "Cutting-edge terahertz technology," vol. 1, no. 2, pp. 97–105, Feb. 2007. [Online]. Available: https://doi.org/10.1038/nphoton.2007.3

[TPS+13] A. Tomasino, A. Parisi, S. Stivala, P. Livreri, A. C. Cino, A. C. Busacca, M. Peccianti, and R. Morandotti, "Wideband THz time domain spectroscopy based on optical rectification and electro-optic sampling," vol. 3, no. 1, Oct. 2013. [Online]. Available: https://doi.org/10.1038/srep03116

[VOM+21] T. Vogel, A. Omar, S. Mansourzadeh, F. Wulf, N. M. Sabanés, M. Müller, T. S. Seifert, A. Weigel, G. Jakob, M. Kläui *et al.*, "Average power scaling of thz spintronic emitters in reflection geometry," *arXiv preprint arXiv:2112.09582*, 2021.

[ZCE06] V. P. Zhukov, E. V. Chulkov, and P. M. Echenique, "Lifetimes and inelastic mean free path of low-energy excited electrons in fe, ni, pt, and au:ab initioGWtcalculations," vol. 73, no. 12, Mar. 2006. [Online]. Available: https://doi.org/10.1103/physrevb.73.125105

[ZTR+13] W. Zouaghi, M. D. Thomson, K. Rabia, R. Hahn, V. Blank, and H. G. Roskos, "Broadband terahertz spectroscopy: principles, fundamental research and potential for industrial applications," vol. 34, no. 6, pp. S179–S199, Oct. 2013. [Online]. Available: https://doi.org/10.1088/0143-0807/34/6/s179

[ZX10] X.-C. Zhang and J. Xu, *Introduction to THz wave photonics*. Springer, 2010, vol. 29.

Appendix A

Measurement of transverse profile of NIR laser beam: knife-edge method

The NIR pump beam size is characterized in the horizontal direction of the beam with the Knife-edge method. The measurement principle is depicted in Fig. A.1. In the knife-edge method, the laser beam is progressively covered

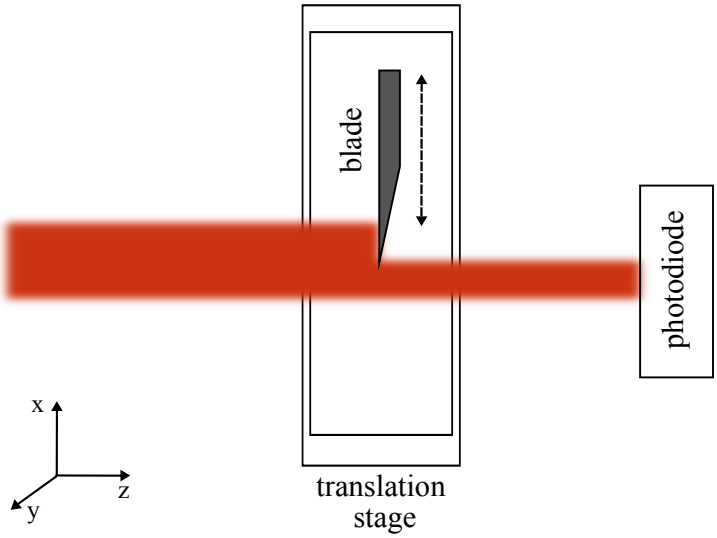

Figure A.1: Measurement principle of knife-edge method.

perpendicular to its optical axis by a sharp edge like a razor-blade, while the transmitted power is measured as a function of the blade's position. The blade is mounted on a one-directional translation stage with a screw-gauge for the position measurement. The power reaches each maximal value when

the beam is not covered by the sharp edge. On the other hand, the measured power is minimal once the beam is fully covered.

The acquired data for all measured beams are shown in Fig. A.2 - Fig. A.6. The data are fitted by the equation:

$$P = \frac{P_{max}}{2}(1 - erf(\frac{\sqrt{2}(x - x_o)}{w_{NIR}})) \tag{A.1}$$

where P_{max} is the maximal power, x_o is the transverse Cartesian coordinate where the beam center is located, erf is the standard error function, and w_{NIR} is the obtained beam radius at the position where the intensity of the beam decreases to $1/e^2$.

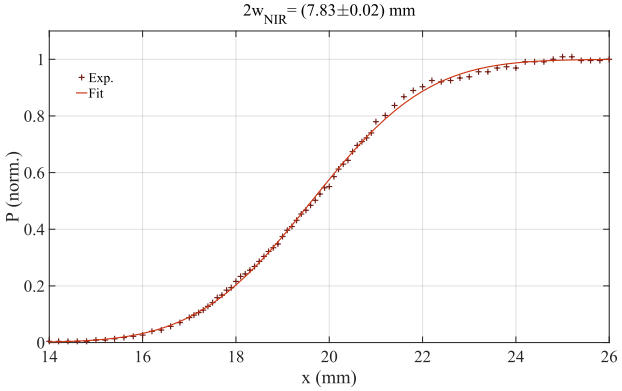

Figure A.2: NIR laser ouput on the pump beam path.

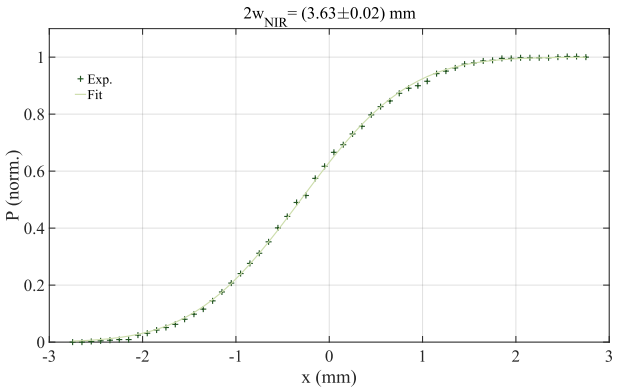

Figure A.3: NIR pump beam realized by Telescope A and Telescope B: Ag plane mirrors.

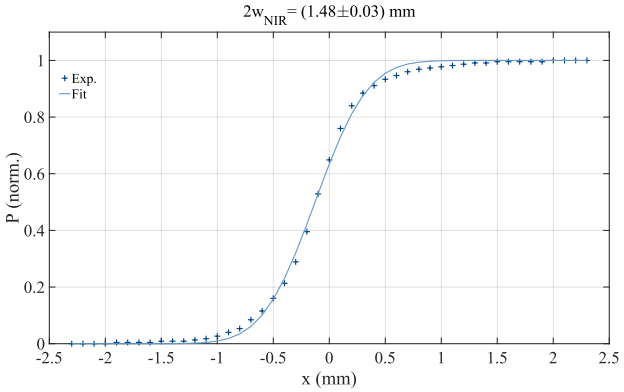

Figure A.4: NIR pump beam realized by Telescope A and Telescope B: Ag concave mirrors of (100+200 mm) EFL

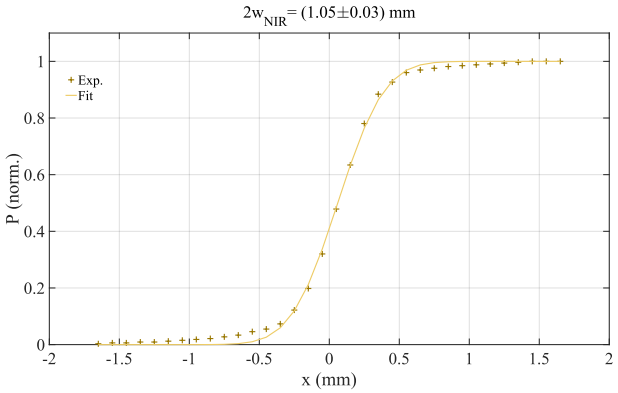

Figure A.5: NIR pump beam realized by Telescope A and Telescope B: Ag concave mirrors of (50+250 mm) EFL

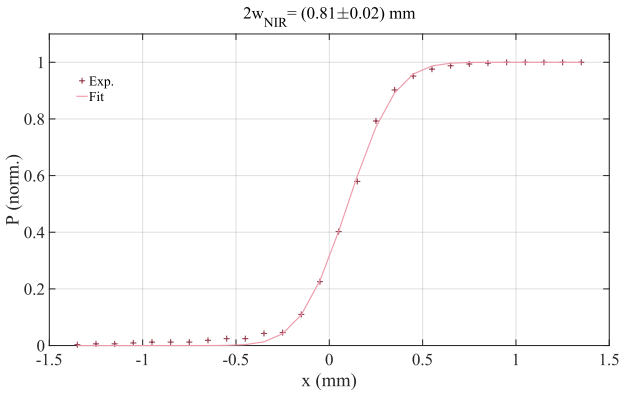

Figure A.6: NIR pump beam realized by Telescope A and Telescope B (moved linear stage): Ag concave mirrors of (50+250 mm) EFL

Appendix B

Mathematical definitions

Fourier Transformation
The Fourier transformation of a function $x(t)$ is given by

$$x(\omega) = \mathcal{F}[x(t)](\omega) = \frac{1}{\sqrt{2\pi}} \int dt x(t) e^{i\omega t} \tag{B.1}$$

The inverse Fourier transformation of a function $y(\omega)$ is given by

$$x(t) = \mathcal{F}^{-1}[x(\omega)](t) = \frac{1}{\sqrt{2\pi}} \int d\omega x(\omega) e^{-i\omega t} \tag{B.2}$$

Convolution
The convolution of two functions $(x * y)(t)$ is defined as

$$(x * y)(t) := \frac{1}{\sqrt{2\pi}} \int dt' x(t - t') y(t') = (y * x)(t) \tag{B.3}$$

Appendix C

Supplementary figures of Chapter 4

C.1 THz waveforms and corresponding spectral amplitudes

C.1.1 Measured THz waveforms versus power

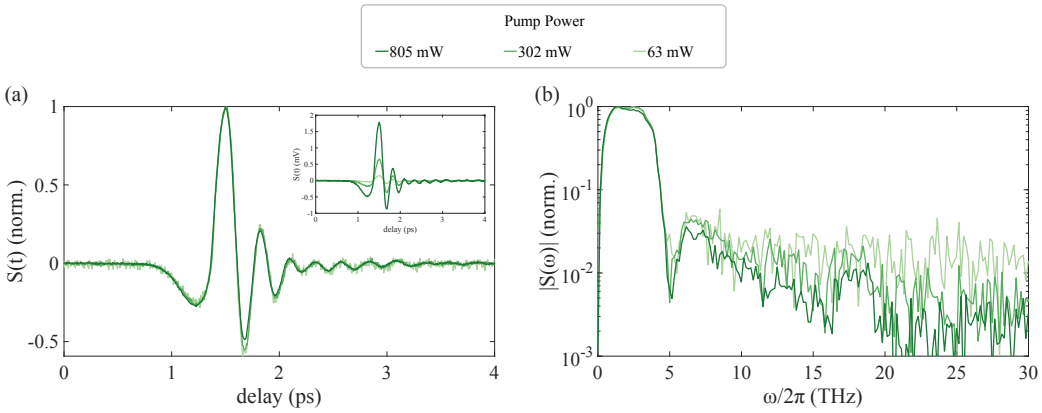

Figure C.1: (a)Electro-optic signals S(t) of THz pulses with their (b) resulting spectral amplitudes $|S(\omega)|$ normalized to their peak values. The THz waveforms are obtained after excitation with **3.63 mm NIR pump spot size**, at high, intermidiate and low pump power, and 1 MHz repetition rate operation. Inset: Not normalized electro-optic signals S(t) of the THz pulses.

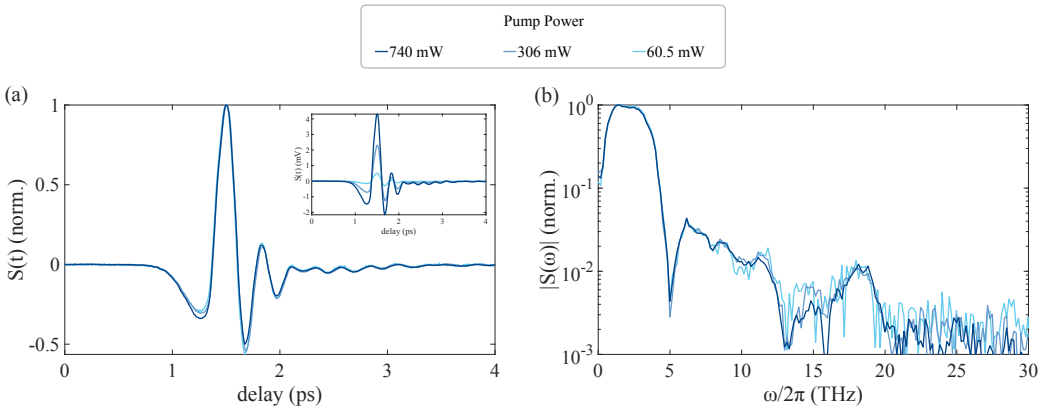

Figure C.2: (a)Electro-optic signals S(t) of THz pulses with their (b) resulting spectral amplitudes $|S(\omega)|$ normalized to their peak values. The THz waveforms are obtained after excitation with **1.48 mm NIR pump spot size**, at high, intermediate, and low pump power, and 0.5 MHz repetition rate operation. Inset: Not normalized electro-optic signals S(t) of the THz pulses.

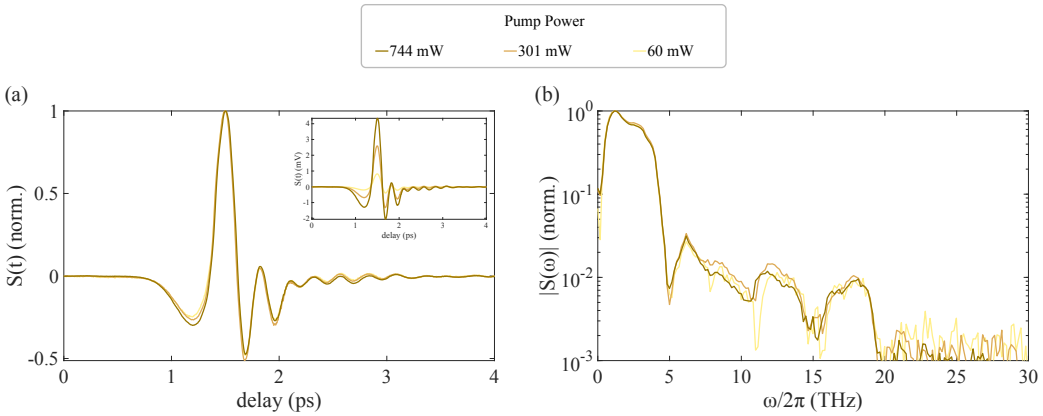

Figure C.3: (a)Electro-optic signals S(t) of THz pulses with their (b) resulting spectral amplitudes $|S(\omega)|$ normalized to their peak values. The THz waveforms are obtained after excitation with **1.05 mm NIR pump spot size**, at high, intermediate, and low pump power, and 0.5 MHz repetition rate operation. Inset: Not normalized electro-optic signals S(t) of the THz pulses.

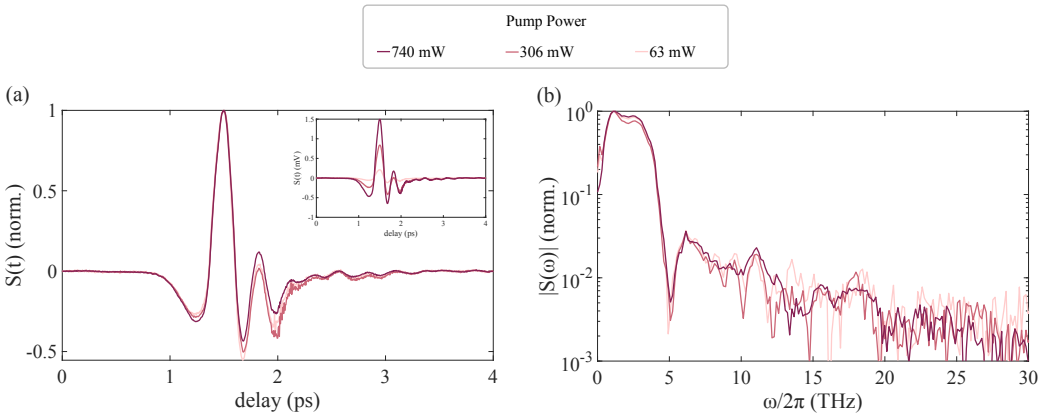

Figure C.4: (a)Electro-optic signals S(t) of THz pulses with their (b) resulting spectral amplitudes $|S(\omega)|$ normalized to their peak values. The THz waveforms are obtained after excitation with **0.81 mm NIR pump spot size**, at high, intermediate, and low pump power, and 1 MHz repetition rate operation. Inset: Not normalized electro-optic signals S(t) of the THz pulses.

C.1.2 Reference THz waveforms

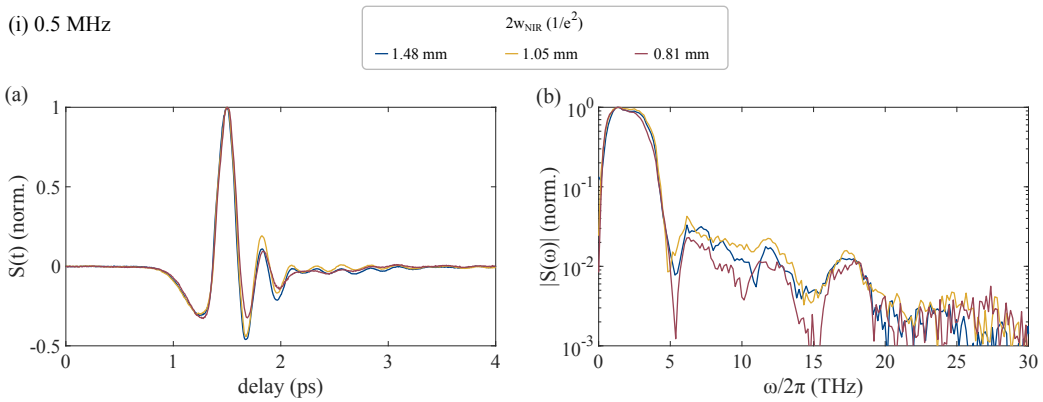

Figure C.5: (a)Electro-optic signals S(t) of THz pulses with their (b) resulting spectral amplitudes $|S(\omega)|$ normalized to their peak values. The THz waveforms are obtained after excitation with three different NIR pump spot sizes at 0.5 MHz repetition rate operation.

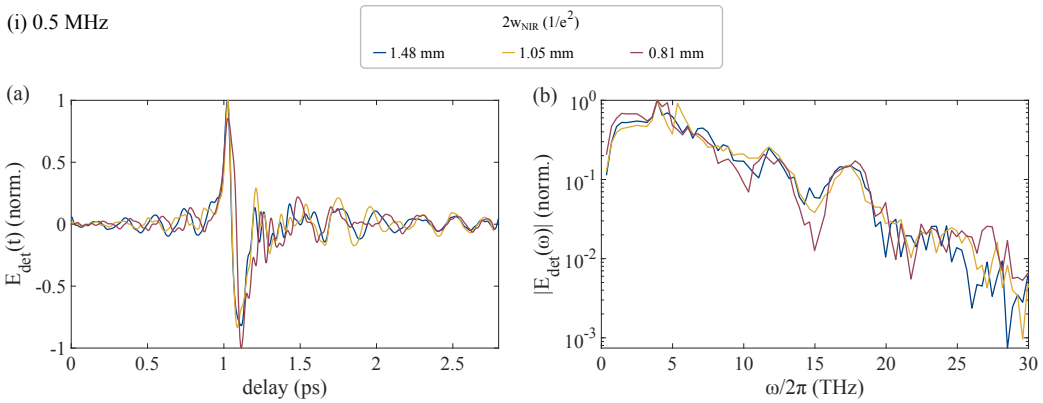

Figure C.6: (a) Deconvoluted THz waveforms incident onto the detector with (b) their corresponding spectral amplitudes normalized to their peak values for the three different employed NIR pump spot sizes at 0.5 MHz repetition rate operation.

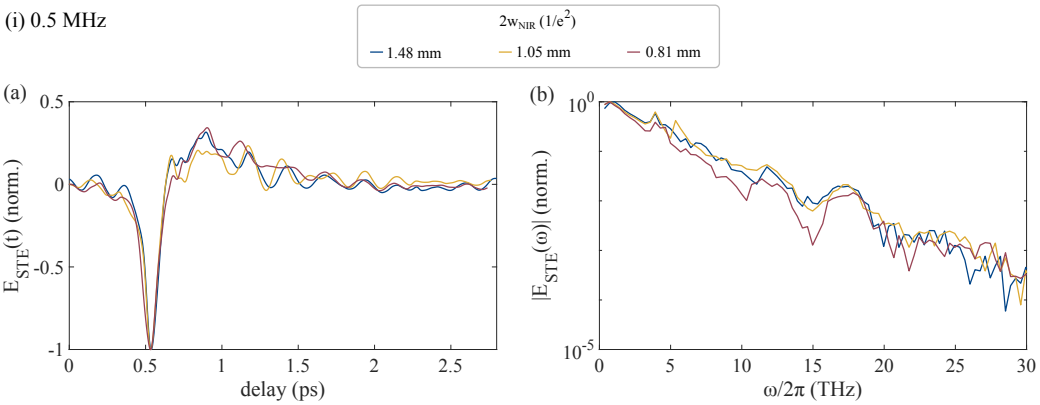

Figure C.7: (a) Deconvoluted THz waveforms emitted by the STE with (b) their corresponding spectral amplitudes normalized to their peak values for the three different employed NIR pump spot sizes at 0.5 MHz repetition rate operation.

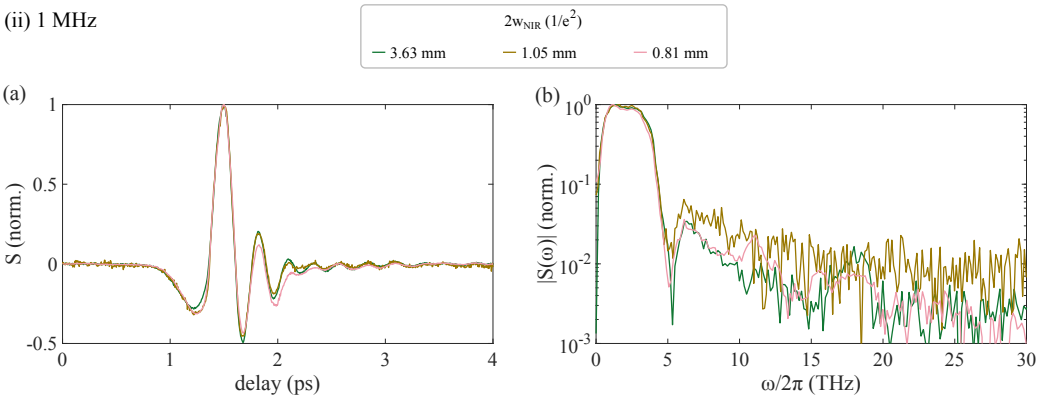

Figure C.8: (a)Electro-optic signals S(t) of THz pulses with their (b) resulting spectral amplitudes $|S(\omega)|$ normalized to their peak values. The THz waveforms are obtained after excitation with three different NIR pump spot sizes at 1 MHz repetition rate operation.

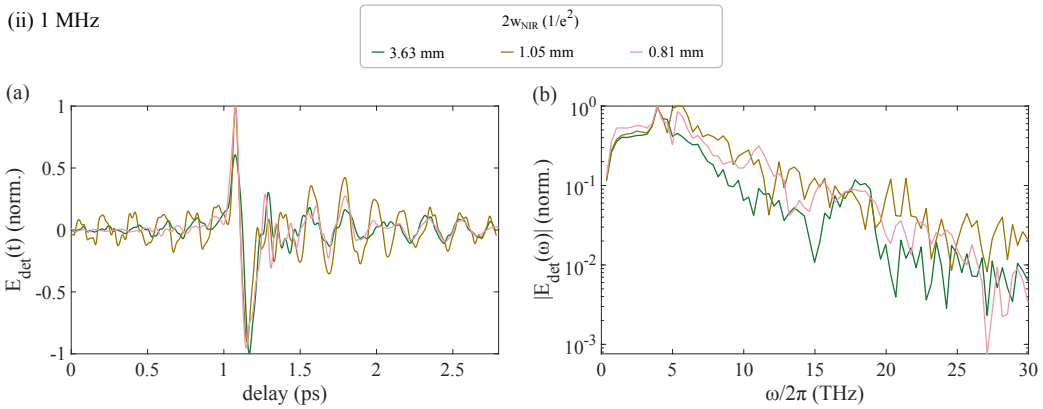

Figure C.9: (a) Deconvoluted THz waveforms incident onto the detector with (b) their corresponding spectral amplitudes normalized to their peak values for the three different employed NIR pump spot sizes at 1 MHz repetition rate operation.

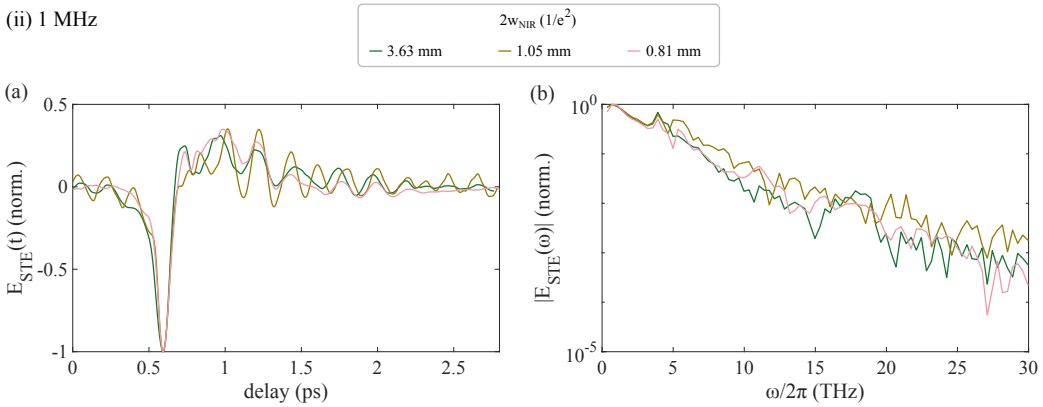

Figure C.10: (a) Deconvoluted THz waveforms emitted by the STE with (b) their corresponding spectral amplitudes normalized to their peak values for the three different employed NIR pump spot sizes at 1 MHz repetition rate operation.

C.2 Numerical simulations

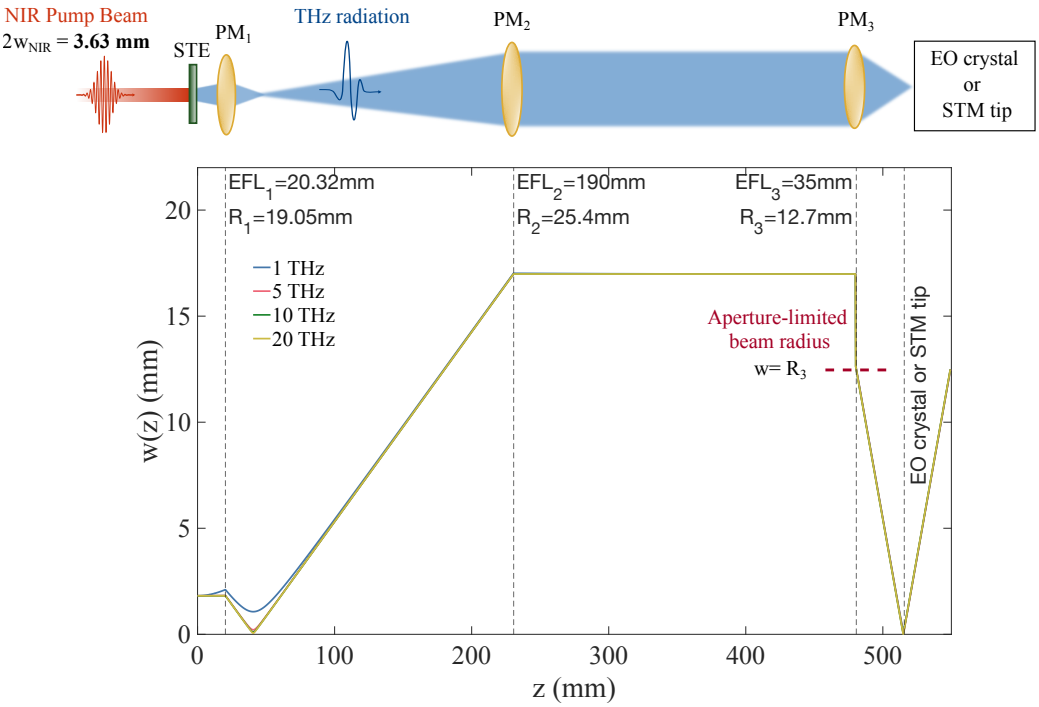

Figure C.11: Assuming a NIR pump beam diameter of 3.63 mm, the beam radius w(z) for four selected THz frequencies along the propagation axis z is numerically calculated and plotted. The sketch above the graph is a visual description of the THz generation and propagation through the simulated optical system.

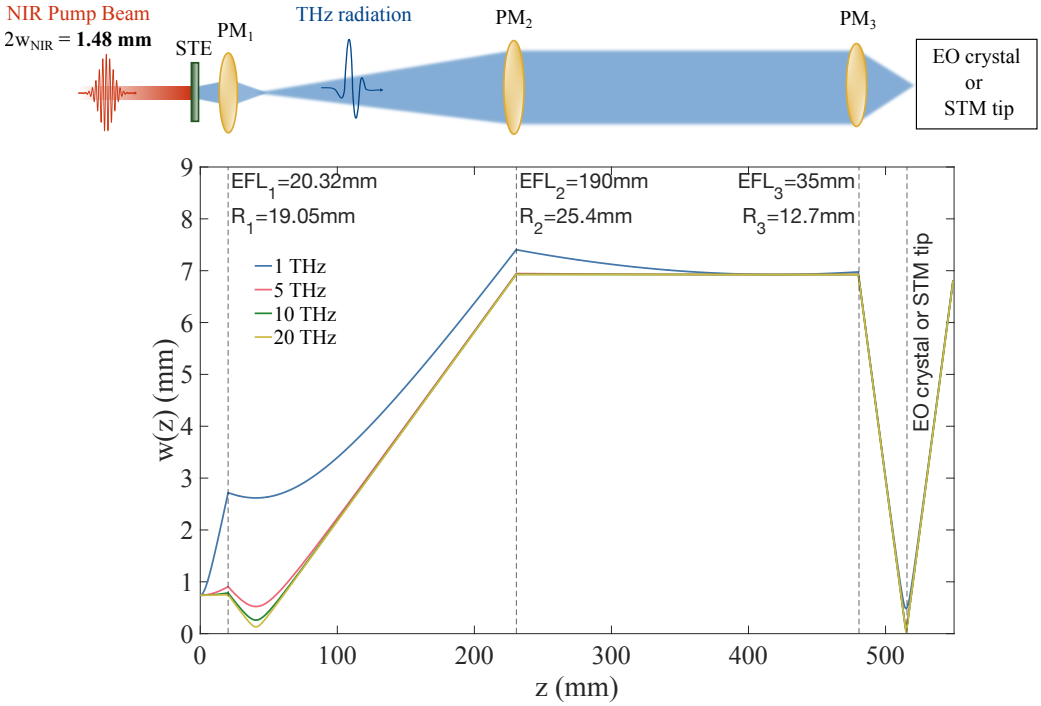

Figure C.12: Assuming a NIR pump beam diameter of 1.48 mm, the beam radius w(z) for four selected THz frequencies along the propagation axis z is numerically calculated and plotted. The sketch above the graph is a visual description of the THz generation and propagation through the simulated optical system.

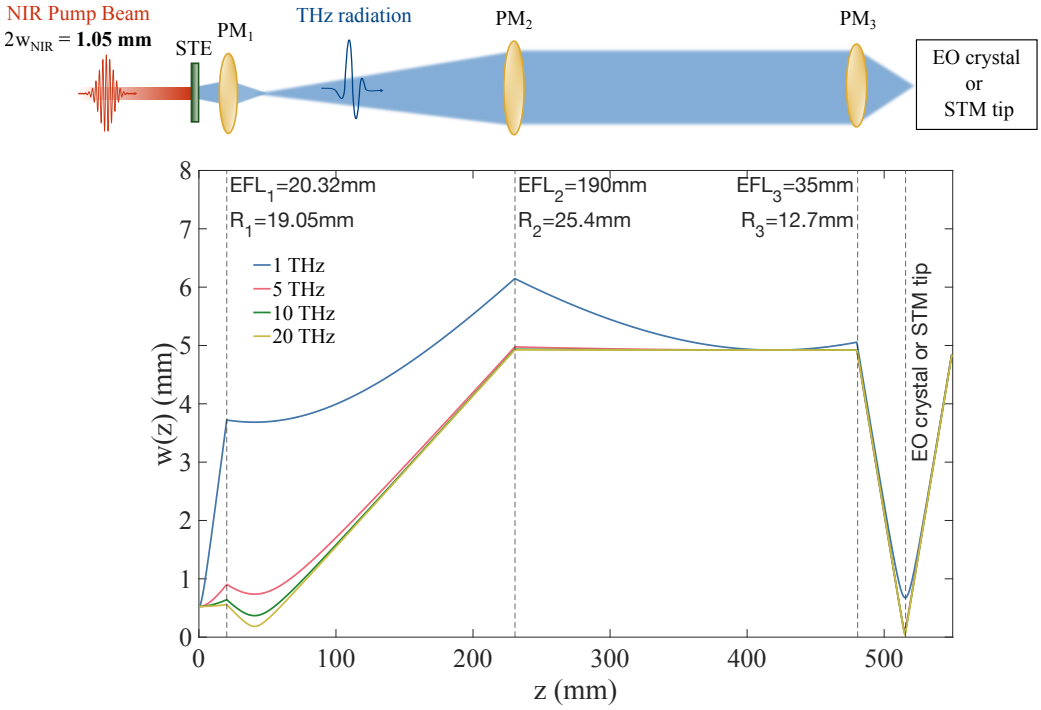

Figure C.13: Assuming a NIR pump beam diameter of 1.05 mm, the beam radius w(z) for four selected THz frequencies along the propagation axis z is numerically calculated and plotted. The sketch above the graph is a visual description of the THz generation and propagation through the simulated optical system.

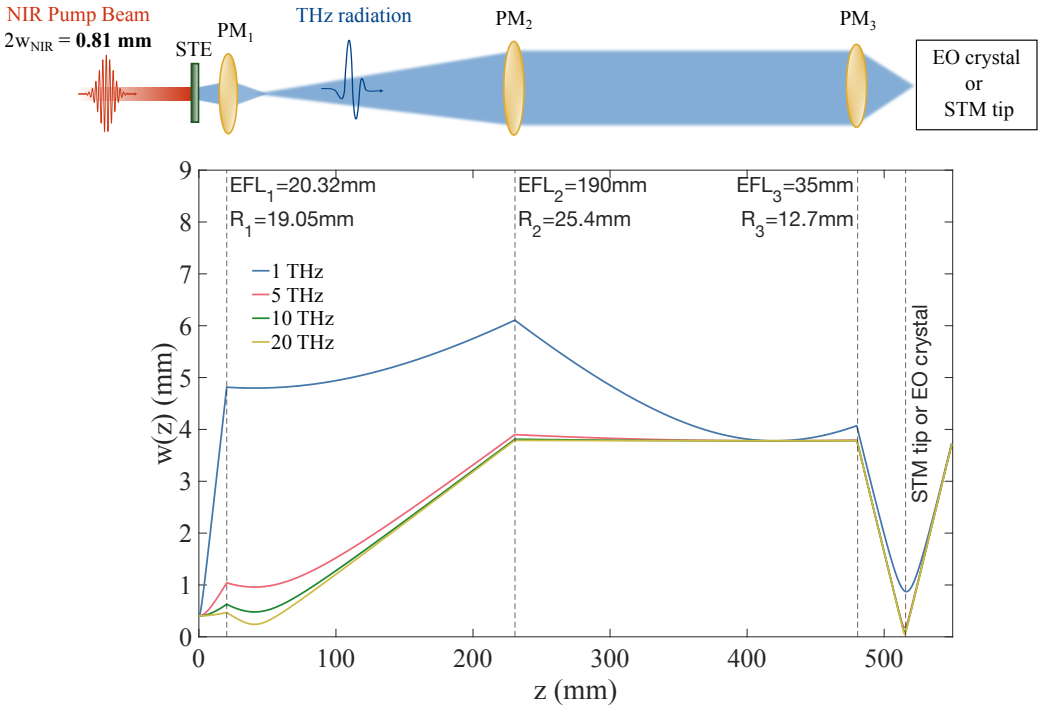

Figure C.14: Assuming a NIR pump beam diameter of 0.81 mm, the beam radius w(z) for four selected THz frequencies along the propagation axis z is numerically calculated and plotted. The sketch above the graph is a visual description of the THz generation and propagation through the simulated optical system.

Acknowledgements

The support of many people made this work possible.

I would like to thank my supervisor Prof. Dr. Tobias Kampfrath, for introducing me to Dr. Melanie Müller, and both for giving me the opportunity to work with them. I thank him for his support during my studies. I am really grateful for the well-organized courses he offers at the university and his great ability to make complex material seem simple. I learned a lot from him during my studies.

Many other special thanks go to Dr. Melanie Müller for providing me the opportunity to work at her research group. I thank her for her constant supervision, her meaningful support, and all the joyful scientific discussions. Above all, I am really grateful for the space she provided me, where I could always ask any question without hesitation and learn a lot from her.

I would further like to thank all the members of our group. I would like to give special thanks to a former member, Natalia Martín Sabanés. She welcomed me very warmly in the group and in the institute. On top of that, I shared my first steps in a scientific laboratory with her. I am really thankful for the support she offered me during that period, which helped me feel less intimidated by the complexity of the lab. Furthermore, I want to thank Fabian Schulz for taking some extra necessary measurements when I could not. Our work in the lab did not overlap, but he was always available to provide his help whenever I needed it and to support me in times of frustration. Also, I want to thank Vivien Sleziona for helping to build the first two telescopes of the new experimental setup. Moreover, I want to thank her for the support, effort, and time she spent reading my thesis and giving me feedback.

The presence of two other people inside the lab was really crucial for me. Faruk Krecinic and Ivana Lapšanská were always willing to help and teach me whenever I needed it, especially at the moments that the laser did not want to work. I would like to thank especially Ivana, for patiently teaching

me and supervising me on how to align the oscillator.

I would also like to thank the whole PC department of the Fritz Haber Institute for providing such a friendly working atmosphere.

I want to thank my friends Gabriela Luna Amador and Giulia Carini for their support and being around whenever I needed them. We have shared countless ups and downs from the first days that we moved to Berlin. Their presence all these years is more than important.

Haydar Altuğ Yıldırım, there is not much that I can say in such a text. Thank you for the patience and all the changes we experience together.

Special thanks are also going to people that it is hard to name here. Still, they are out there, and with their stance and with the example of their lives, teach me qualities and give me great hope -necessary to keep going-, that any institution could ever provide me.

Finally, I want to thank my sweet family. My mother, father, brother, and grandmother simply for their endless love.

Declaration

I, Alkisti Vaitsi, declare that this master thesis is solely my work. Parts taken directly or indirectly from previous works are indicated in the references section completely. This work is not submitted to another academic institution or not published previously.

Berlin, January 24, 2022

Alkisti Vaitsi